DESIGN OF A DUAL-EXCITED SYNCHRONOUS MACHINE AND DEVELOPMENT OF STABILIZATION TECHNIQUES

by

Eugene Peter Dick

B.A.Sc., University of Waterloo, 1971

A THESIS SUBMITTED IN PARTIAL FULFILMENT OF

THE REQUIREMENTS FOR THE DEGREE OF

MASTER OF APPLIED SCIENCE

in the Department

of

Electrical Engineering

We accept this thesis as conforming to the required standard

THE UNIVERSITY OF BRITISH COLUMBIA

August 1973

In presenting this thesis in partial fulfilment of the requirements for an advanced degree at the University of British Columbia, I agree that the Library shall make it freely available for reference and study. I further agree that permission for extensive copying of this thesis for scholarly purposes may be granted by the Head of my Department or by his representatives. It is understood that copying or publication of this thesis for financial gain shall not be allowed without my written permission.

Department of Electrical Engineering

The University of British Columbia
Vancouver 8, Canada

Date Aug. 10/73

ABSTRACT

A dual-excited synchronous machine is designed and constructed. A power system is simulated using the machine and a medium length transmission line joined to the laboratory bus energized from B.C. Hydro which is considered the infinite bus. The effect of supplemental excitation control on power system stability is investigated. Feedback control is used in both the direct and quadrature fields. Torque angle, speed, power and terminal current signals are compared in their damping action. The response is also calculated from a ninth order mathematical model. It is found that the shaft speed is the best supplemental signal and that the direct and quadrature fields are equally effective in dynamically controlling the machine when operating near rated output.

TABLE OF CONTENTS

Page

LIST OF TABLES

LIST OF ILLUSTRATIONS

ACKNOWLEDGEMENT

I am grateful to all the people who assisted in the completion of this thesis. My supervisor, Dr. Y.N. Yu, patiently worked through the experimental problems as they developed and provided invaluable direction during the writing period. I also wish to thank Dr. H. Cheann and B. Habibullah for their helpful comments while reviewing the draft.

The machining and fabrication of the generator were done by Derrik Daines and his excellent workmanship resulted in a flawless operating record. My appreciation to Mr. H.T. Walters for ordering the electronic components and Al MacKenzie for locating instruments and miscellaneous parts. The photographs were done by Mr. H.H. Black and the typing by Norma Duggan. Finally, I wish to thank fellow graduate students and other faculty members for the encouragement and experience shared during the last two years.

NOMENCLATURE

Note: Upper case symbols indicate MKS units; lower case symbols indicate per unit quantities.

General

P	derivative operator, d/dt
o	subscript denoting initial condition
Δ	prefix denoting a linearized variable
ω_o	synchronous speed, 377 rad/s

Synchronous Machine

b,g,r,x	transmission line parameters
D,d	natural damping
I_d, i_d, I_q, i_q	D and Q axis armature current
$I_{fd}, i_{fd}, I_{fq}, i_{fq}$	D and Q axis field current
I_t, i_t	magnitude of armature current
I_{fb}, I_{nb}	base field and armature current
J	rotor inertia
P, P_e	electrical power
Q	reactive power
R_a, r_a	armature resistance
$R_{fd}, r_{fd}, R_{fq}, r_{fq}$	D and Q axis field resistance
T_e, T_m, t_m	electrical and mechanical torque
T_b	base torque
T_{do}', T_{qo}'	D and Q axis open circuit transient time constant
U_d, u_d, U_q. u_q	D and Q axis generated voltage
V_d, v_d, V_q, v_q	D and Q axis terminal voltage

$V_{fd}, v_{fd}, V_{fq}, v_{fq}$	D and Q axis field voltage
V_t, v_t	magnitude of terminal voltage
V_o, v_o	infinite bus voltage
V_{fb}, V_{nb}	base field and armature voltage
$X_{afd}, X_{fad}, x_{md}, X_{afq}, X_{faq}, x_{mq}$	D and Q axis mutual reactance
X_d, x_d, X_q, x_q	D and Q axis synchronous reactance
X_d', x_d', X_q', x_q'	D and Q axis transient reactance
$X_{ffd}, x_{fd}, X_{ffq}, x_{fq}$	D and Q axis field reactance
Z_{fb}, Z_{nb}	base field and armature impedance
δ	torque angle
θ	power factor
Ψ_d, ψ_d, Ψ_q, ψ_q	D and Q axis flux linkage
ψ_{fd}, ψ_{fq}	D and Q axis field flux linkage
ω	shaft speed

Control System and Exciter

i_a, i_b	phase A,B line current
i_f	field current
K	exciter gain
K_{P1}, K_{P2}	voltage regulator and supplemental control gain
K_T	transducer gain
L_f, L_f'	conventional and modified field inductance
L_s	search coil inductance
M	field to search coil mutual inductance
R_f, R_f'	conventional and modified field resistance

R_x	field current sampling resistor
T_f'	modified field time constant
$T_1 \ldots T_6$	regulator time constants
u	supplemental input signal
v_{ac}, v_{bc}	line terminal voltage
v_i	exciter input voltage
V_{REF}	voltage regulator reference

1. INTRODUCTION

There has been widespread interest in the use of dual field synchronous machines having two independent windings on the rotor. In 1962, Hamdi-Sepen proposed that a second winding be temporarily energized during severe disturbances giving improved transient stability [1]. Two years later, Botvinnik described how such a machine could be operated at different slip speeds, eliminating the problem of synchronous stability [2].

Between 1968 and 1970 a large number of papers examined the theoretical advantages of dual axis machines. Takata confirmed that a two-axis machine is more effective in controlling bus voltage fluctuation than a single-axis machine [3]. In a second paper he applied the maximum principle to derive a bang-bang optimal control of dual field voltage to effectively suppress machine hunting [4]. Soper and Fagg showed that torque and reactive requirements can be separately controlled, that machine stability is not reduced at leading power factor and that the speed of response to transients is twice that of a conventional machine [5]. Robinson extended this analysis to prove that the dual field machine has no transient saliency resulting in good transient stability performance [6]. Krause and Towle compared the damping characteristics of a two-field machine to a one-field machine at varying torque angles and emphasized the use of proper controller compensation [7].

More recently, the emphasis in Canada has shifted to control design for the dual field generator. Subramaniam and Malik at Calgary used dynamic optimization techniques to determine the optimum control for a seventh order model [8]. El-Serafi and Badr in Saskatoon have

chosen excitation control parameters which enable a machine to develop maximum possible capacitive power [9].

This thesis compares the relative effectiveness of torque angle, speed, electrical power and terminal current feedback in dynamically damping machine oscillations. For each signal the proper compensation is designed and the output is applied to the direct and quadrature field windings in turn. There is always a voltage regulator used on the direct field. The quadrature field excitation is zero in steady state operation. Other studies have demonstrated the superior characteristics of the quadrature winding when the machine is operating at low power and high capacitive load. Here other differences between the windings are investigated by operating at high power and small reactive load.

The study in this thesis is conducted on both a laboratory micromachine and a mathematical model of the ninth order. The micromachine is a modified wound rotor induction motor with the wound rotor acting as the synchronous machine armature. The two field windings are located on the stator and their design is described in Chapter 2. The design of torque angle and speed sensing circuits are discussed in Chapter 3.

2. DUAL FIELD SYNCHRONOUS MACHINE DESIGN AND PARAMETER TESTS

2.1 Tamper Set

The dual-field synchronous machine is adapted from the induction machine of the Tamper Set used for undergraduate laboratories. The dc machine of the set is used to simulate a constant torque turbine and the synchronous machine to provide torque angle and frequency signals.

The induction motor is modified into a synchronous generator by designing a new stator with fields on both direct (D) and quadrature (Q) axes but using the existing wound rotor for the armature. This inverted arrangement has the advantage that the rotating member can be readily used without any change and more winding space is available for the stator fields.

Table 2.1 lists the ratings and rotor parameters of the induction motor as supplied by the manufacturer.

Table 2.1

Ratings of Rotor Parameters of the Induction Machine

Horsepower	3.0	Diameter	13.89 cm
Poles	4	Length	9.52 cm
Line voltage	125 V	Air gap	.038 cm
Current	11.0 A	Pole flux	536 K.G.
Resistance/phase at 75°C	.18Ω		

2.2 Pole and Yoke Design of the Synchronous Machine

Salient poles are chosen for the design as distributed windings are too complex to be constructed with university facilities. An

optimum ratio of iron to copper may exist but it is very difficult to calculate due to the non-linearity of saturation in iron. Good results are obtained by limiting the maximum flux density in iron to 15 Kilogauss (K.G.). With rotor slots covering about 50 per cent of the tooth pitch, this criterion is met by choosing the air gap flux density to be seven K.G. Thus the flux per pole is approximately determined by the physical dimensions of the rotor as follows:

$$\phi_P = \frac{2}{\pi} B_g \frac{\pi \ell D}{4} = 231 \text{ Kilo-line} \qquad (2.1)$$

where B_g is the maximum flux density in the air gap, D is the rotor diameter, and ℓ the lamination length.

Terminal voltage, which is proportional to flux per pole, can now be calculated from Table 2.1 and Equation 2.1.

$$V_{phase} = \frac{125}{\sqrt{3}} \frac{231}{536} = 31.1 \text{ V} \qquad (2.2)$$

Thus an autotransformer with ratio 1:4 is required to step up the voltage to 120/208 volts of the laboratory supply.

The cross section of the pole is chosen as 18.5 cm^2 from consideration of the allowable flux density in iron and assuming 20% leakage flux between pole shoes. The stator yoke flux density is 12 K.G. and with flux dividing on entering the yoke, an area of only 11.6 cm^2 is required for each set of poles. The axial length of the yoke is limited to 15 cm by the distance between existing bearing supports, resulting in a yoke thickness of 1.5 cm. Figure 2.1 gives details of the dimensions of magnetic circuit for one pole.

An air gap size of one millimeter is chosen. It is anticipated that approximately 70% of the no load excitation ampere-turn will

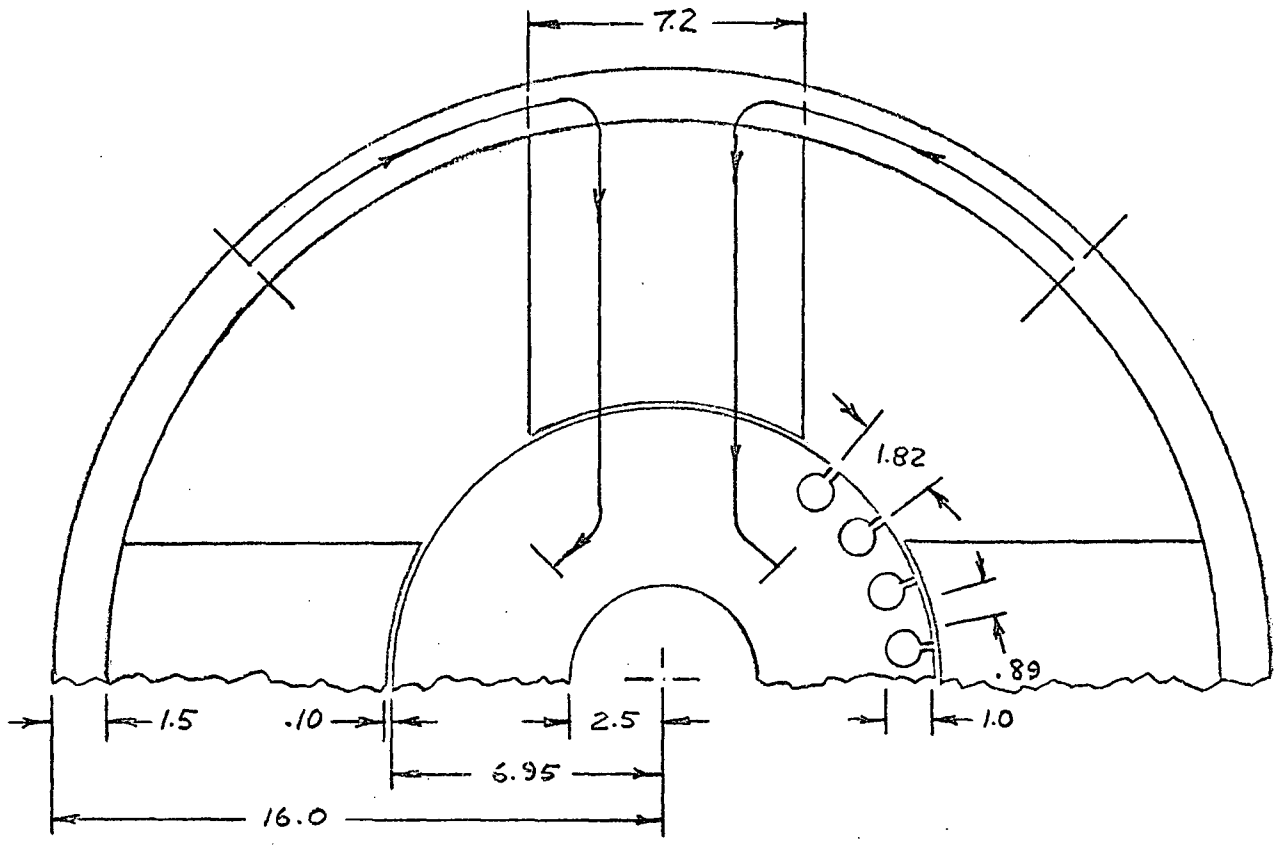

Figure 2.1 Dimensions of Magnetic Circuit

be consumed in this region. The ampere-turn loss for each component of the magnetic circuit is the product of flux path length and magnetic field intensity, H. For the air gap, H equals B_g divided by μ_o, where B_g is the maximum flux density and μ_o the permittivity of free space.

Due to the rotor slot opening, the effective air gap length is increased by a factor of K equal to 1.045 [10]. The calculated ampere-turn loss is 573.

For the iron part of the circuit, H is determined from the B-H curves available in reference [10]. Sheet steel punchings are used on the rotor. Although the flux density in the teeth is high, the tooth length is only one centimeter, resulting in a loss of nine ampere-turn. As shown in Figure 2.1, the flux divides on entering the rotor yoke, producing a flux density of 7.3 K.G. Neglecting the shaft, the rotor yoke length is 5.0 cm with a loss of seven ampere-turn.

The pole is made of mild steel and a high flux density of 15 K.G. is chosen to provide maximum space for the field windings. With a pole length of 7.5 cm the ampere-turn loss is 127. The stator yoke is made of the same material with a magnetic circuit length per pole of 12.7 cm. The flux density is lower than in the pole resulting in 115 ampere-turn. The total ampere-turn per pole is 914 allowing 10 per cent for armature reaction.

2.3 Field Windings

The winding area depends on the required excitation, the maximum allowable insulation temperature and the ability of the winding to dissipate heat. In this design, a current density of 250 amp cm^{-2} is used, requiring a copper cross section of 3.7 cm^2 and a winding area of about 6.1 cm^2. The winding length is chosen as 3.6 cm, allowing space for the pole shoe, damper winding search coil, and insulation. The two sets of field windings and poles are placed at opposite ends of the stator, each set occupying 7.5 cm. The space remaining for the

pole body is 2.8 cm. Thus the pole width in the tangential direction is 7.2 cm to provide the required pole area. The four corners of the pole body are bevelled by 1.3 cm and .7 cm to reduce the winding turn length. One of the eight poles is shown in Figure 2.2.

The mean turn length (MTL), calculated from the geometry of the winding, is 26.4 cm. The design winding resistance (R_w) is one ohm per pole so that the exciter amplifier is loaded by four ohms. The conductor cross section (A_c) is given by:

$$A_c = \sqrt{\frac{\rho A_w MTL}{R_w}} = 1.4 \times 10 \text{ cm}^2 \qquad (2.3)$$

where ρ is the conductor resistivity and A_w the total copper cross section. Wire size AWG #16 is used with a diameter of .14 cm including insulation.

The number of turns per pole is decided by the winding space, 1.7 cm by 3.6 cm, and wire size with 25 turns per layer and 12 layers resulting in 300 turns. To provide the 914 ampere-turns requires a field current of about 3.0 amps and a voltage drop of 12 volts for the four poles. Number 16 wire can handle considerably higher currents temporarily, allowing forced excitation of several per unit. Each winding is subdivided into two coils, as in Figure 2.3, so that it can be easily shaped to fit the stator yoke.

To simulate the field time constant of a large machine, a search coil of 75 turns of AWG #30 wire is embedded between the two main windings and connected to the exciter amplifier. All windings are wrapped in Scotch No. 27 electrical tape and sealed with acrylic spray. Connections are soldered and insulated with heat shrinkable tubing.

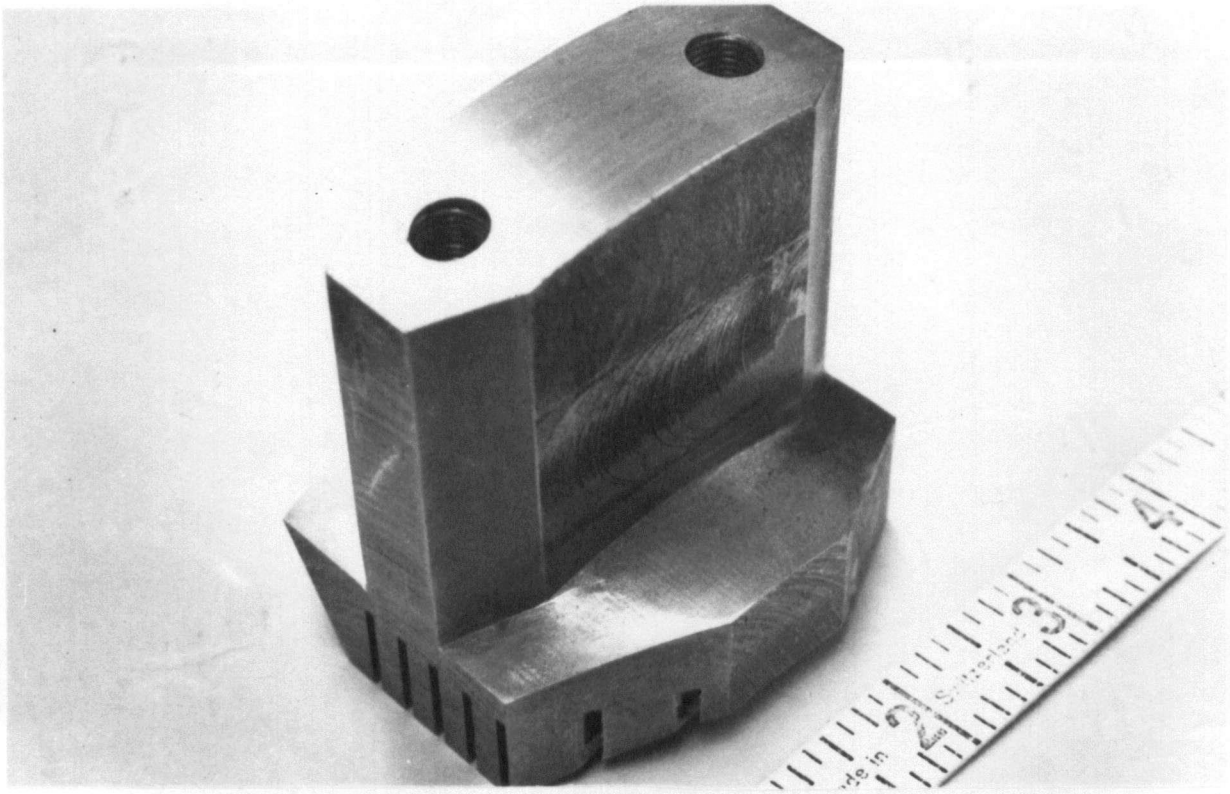

Figure 2.2 Pole Piece for Dual Field Machine

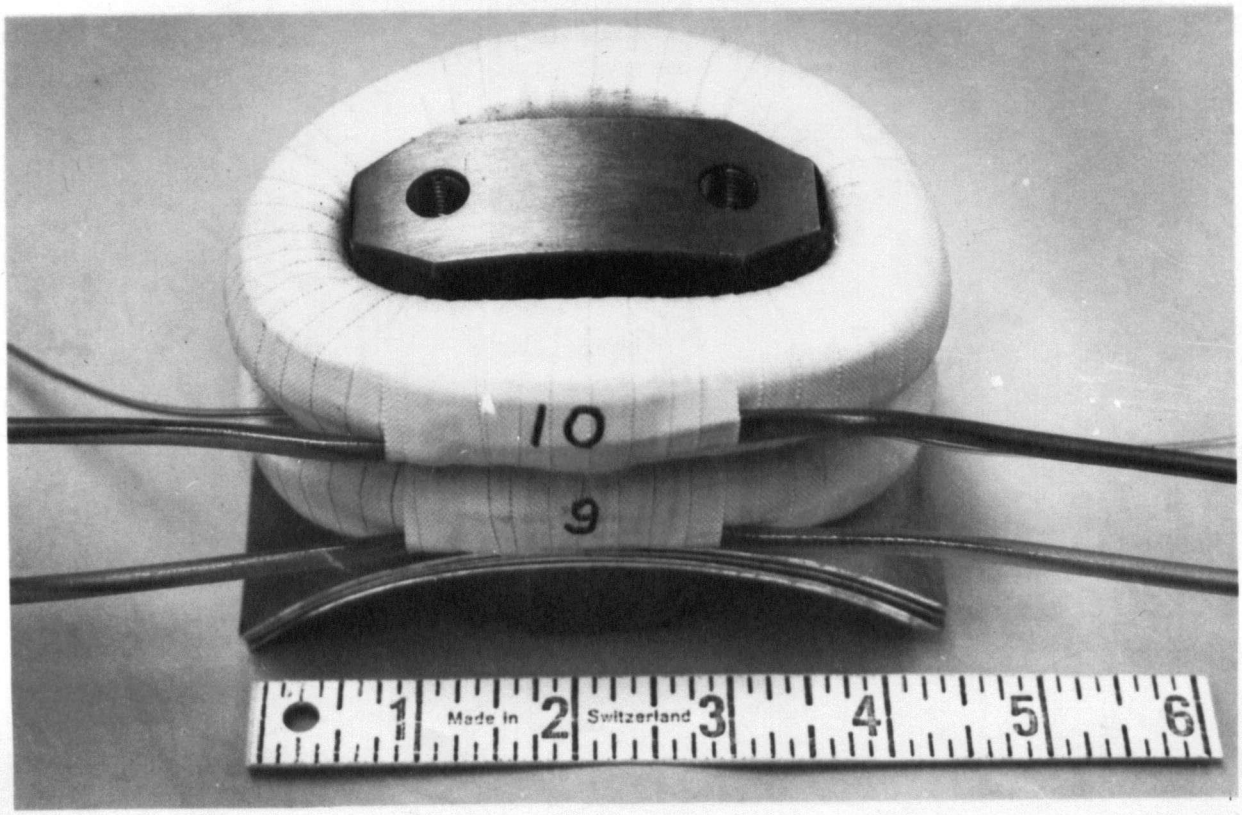

Figure 2.3 Field and Damper Windings

2.4 Pole Shoe

The pole shoe design determines the air gap flux distribution which in turn affects the harmonic content of the output voltage. Two dimensions are variable. The first is the axial shoe length. With D and Q poles adjacent at the midpoint of the machine, leakage flux is minimized by clipping the shoe corners, leaving a gap of 1.6 cm. As shown in Figure 2.2, the shoe narrows away from the centerline with armature voltage decreased accordingly.

The second variable dimension is the air gap length. For a rotor of radius R_r, a curved shoe surface of radius R_s and a minimum air gap of δ_o, the air gap length at an angle θ from the centerline can be described by

$$\delta(\theta) = \left(R_r - \frac{R_r^2}{R_s} - \frac{R_r \delta_o}{R_s}\right)(1 - \cos\theta) + \delta_o \qquad (2.4)$$

The flux density and hence the induced voltage vary inversely with $\delta(\theta)$ as follows

$$E(\theta) = E_{max} \frac{1 - C}{1 - C \cdot \cos\theta}$$

where

$$C = \frac{R_r - \frac{R_r^2}{R_s} - \frac{R_r \delta_o}{R_s}}{R_r - \frac{R_r^2}{R_s} - \frac{R_r \delta_o}{R_s} + \delta_o} \qquad (2.5)$$

Computational techniques are used to approximate the ideal cosine curve with the effect of shoe clipping and Equation (2.5) combined. The shoe surface radius R_s is then calculated as 7.28 cm.

Laminated structure of the pole is impractical in this case so seven .16 cm slits are machined into the shoe surface to reduce

eddy current losses. Shoulders are provided to support the windings. The dampers, which appear in Figure 2.3, are punched from .16 cm sheet aluminum. An exploded view of the completed machine is shown in Figure 2.4 with the laboratory setup in Figure 2.5.

2.5 Parameter Tests of the Machine Set

Figure 2.6 shows the open and short circuit test results with D and Q field excitation. The reactances X_d, X_q, X_{afd}, X_{afq} are determined directly. The transient reactances X_d' and X_q' are measured by the I.E.E.E. Sudden Short Circuit method while time constants T_{do}' and T_{qo}' are obtained from the Field Short Circuit method. Inertia is calculated from the frequency of shaft oscillations when it is loaded with a known spring constant. Natural damping is mainly due to changes in counter EMF with speed in the dc driving motor. It is determined from the change in shaft speed with removal of a known electrical load on the generator. These results are given in Table 2.2.

Harmonics in output voltage are measured with a tunable voltmeter. The 3rd, 11th, and 13th are larger than one per cent as shown in Table 2.3. The third harmonic is due to pole shaping while the 11th and 13th are caused by the rotor slot opening, 12 slots per pole. The damper windings attenuate the latter under full load.

The effect of the rotor slots could be reduced with a larger air gap, but the machine rating would be decreased. It is assumed that these high frequency harmonics do not influence the transient and dynamic stability study because the natural mechanical oscillation frequency of the machine is about 1.9 Hz.

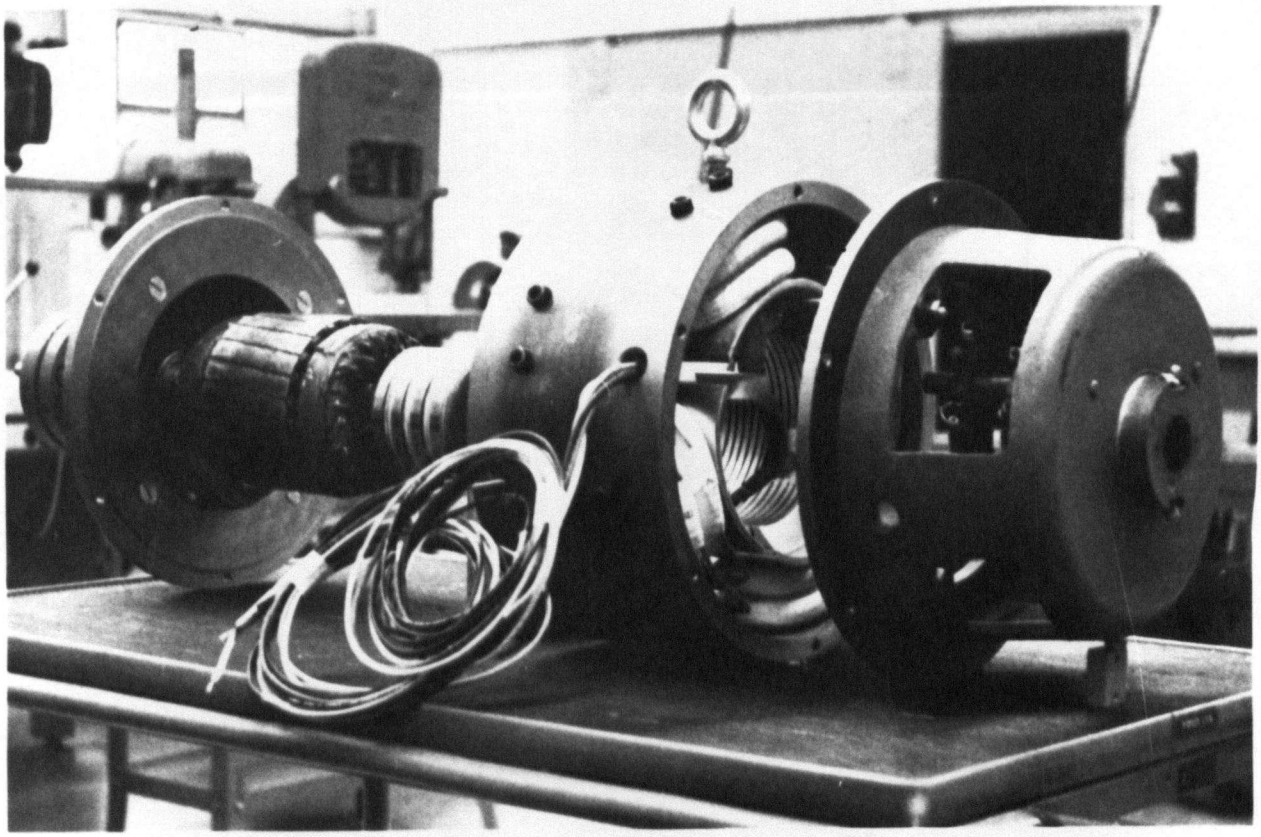

Figure 2.4 Dual Field Machine Before Assembly

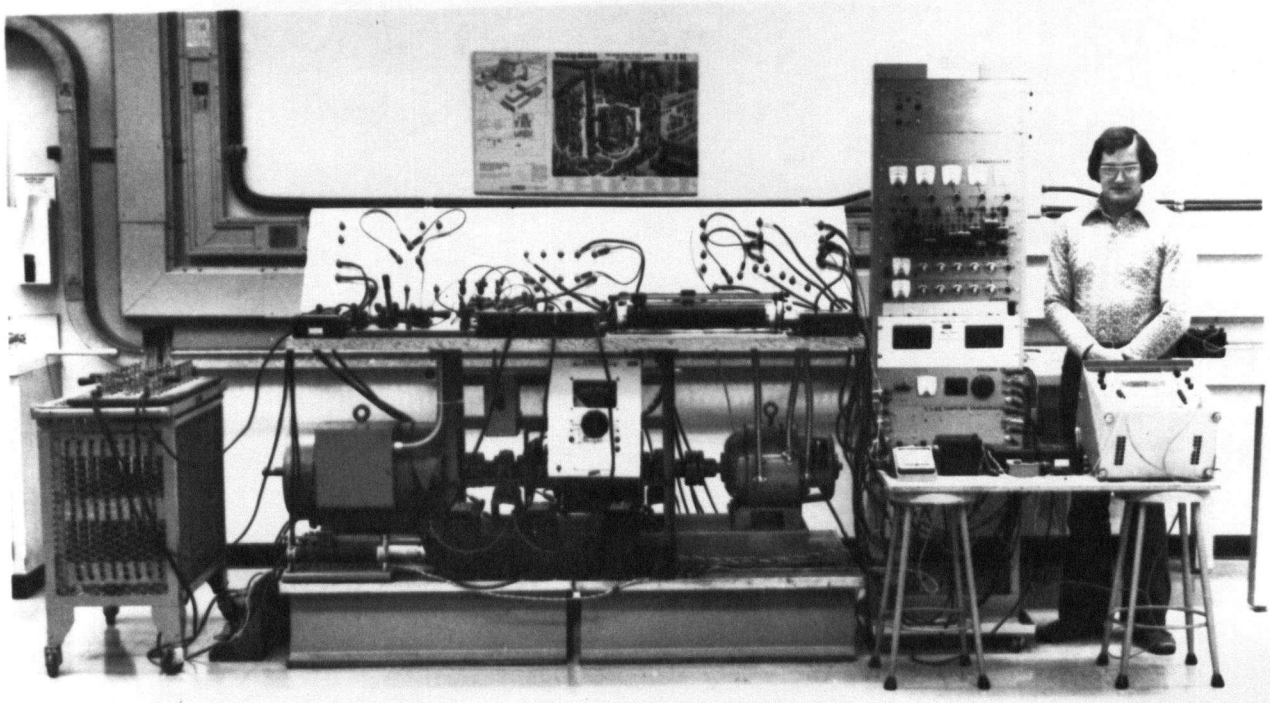

Figure 2.5 Laboratory Setup and Author

Table 2.2

Machine Test Parameters

X_d	2.14 Ω	X_q	1.98 Ω
X_d'	1.20 Ω	X_q'	1.20 Ω
X_{afd}	11.1 Ω	X_{afd}	10.0 Ω
T_{do}'	2.3 sec	T_{qo}'	2.3 sec
J	.040 nt.m.sec^2	D	.053 nt.m.sec

Table 2.3

Terminal Voltage Harmonics (Per Cent)

	No Load D	No Load Q	Full Load D	Full Load Q
3rd	4.5	4.0	9.0	12.0
11th	6.4	6.5	1.9	3.0
13th	2.5	1.7	1.5	.9

3. INSTRUMENTATION AND CONTROL PANELS

Supplemental excitation control requires accurate, low noise and fast responding transducers. In this chapter, devices for measuring torque angle, speed, terminal voltage, current and electrical power are developed. Also described are means for signal compensation and a high speed electronic exciter.

3.1 Torque Angle Transducer

The transducer provides a dc output signal proportional to the torque angle between the generator Q axis and the infinite bus of the system represented by the laboratory supply. The significant features of the transducer are:

1. linear characteristic in the range 0 - 2π radian
2. noise of 360 Hz under .03 radian
3. time lag less than 20 msec.

The linearity is checked within the steady state stability limit of the machine. The true torque angle is measured on a dual channel oscilloscope from the zero crossing of voltages of the original synchronous machine and the laboratory supply. Results between 0 and 60 degrees are recorded in Figure 3.1. Resolution is limited by drift in torque angle caused by power supply disturbances feeding the drive motor.

The transducer operates as follows. The original synchronous machine of the Tamper Set converts shaft position into three-phase induced voltages. These signals and the three bus voltages of the laboratory supply are reduced and applied to six comparators which sense zero crossings and output 0 - 5 volt logic levels. Figure 3.2 describes the logic for one of three phases.

A hexinverter integrated circuit makes available the logical

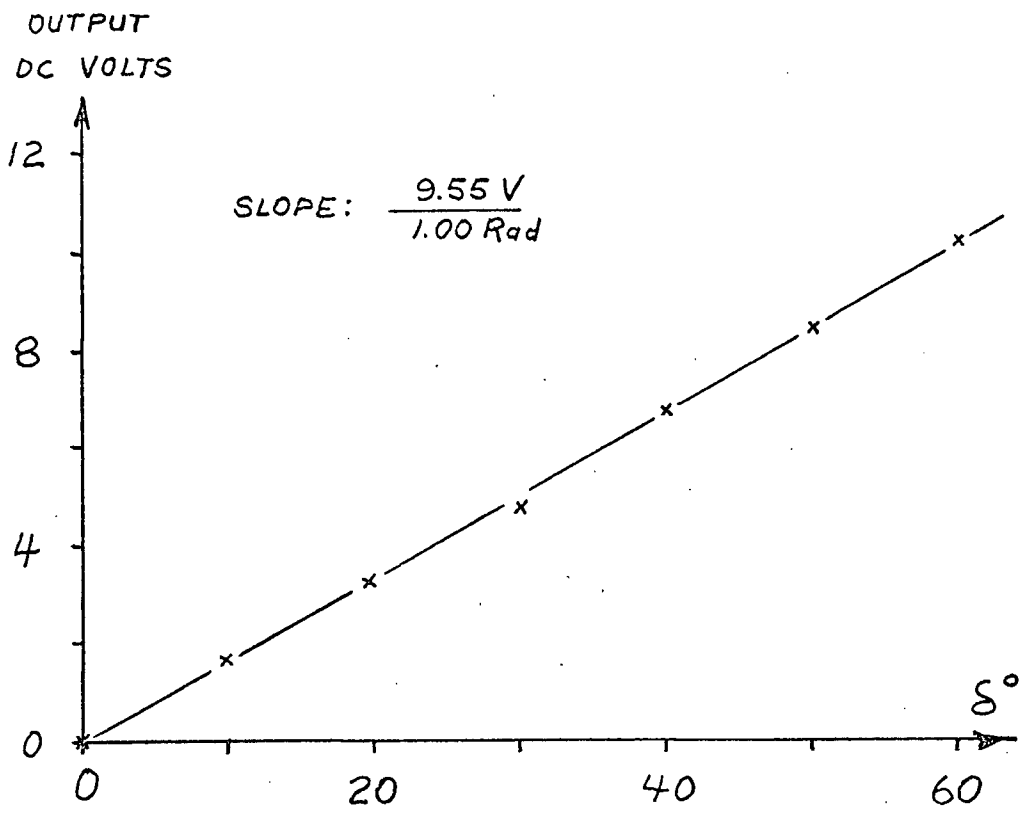

Figure 3.1 Torque Angle Transducer Transfer Characteristic

complements $\bar{a}$ and $\bar{a}'$ from inputs a and a'. The four signals enter two Reset-Set (RS) flip-flops with outputs u,v,w and x summed in the analog sense to Z. The pulses in Z are constant in amplitude with width equal to input voltage phase difference. Inclusion of all three phases gives 360 pulses per second. A 12 dB per octave low pass filter with cutoff at 60 Hz smoothes the output. The complete wiring schematic is given in Figure 3.3.

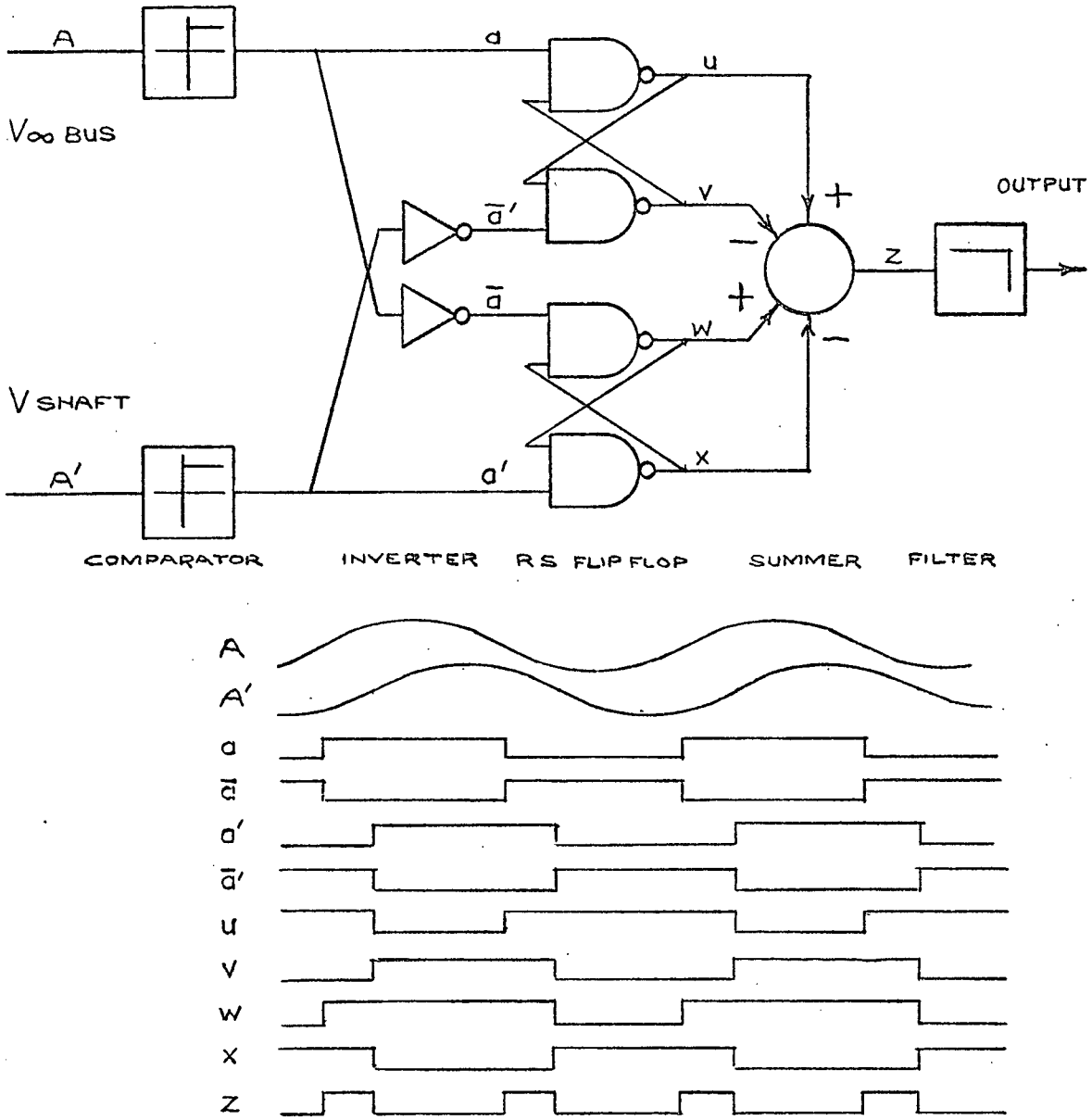

Figure 3.2 Block Diagram of Torque Angle Transducer

3.2 Speed Transducer

Relatively large swings in torque angle are reflected in only small changes in shaft speed; thus requiring a speed transducer of high sensitivity. Conventional tachometer generators and digital methods

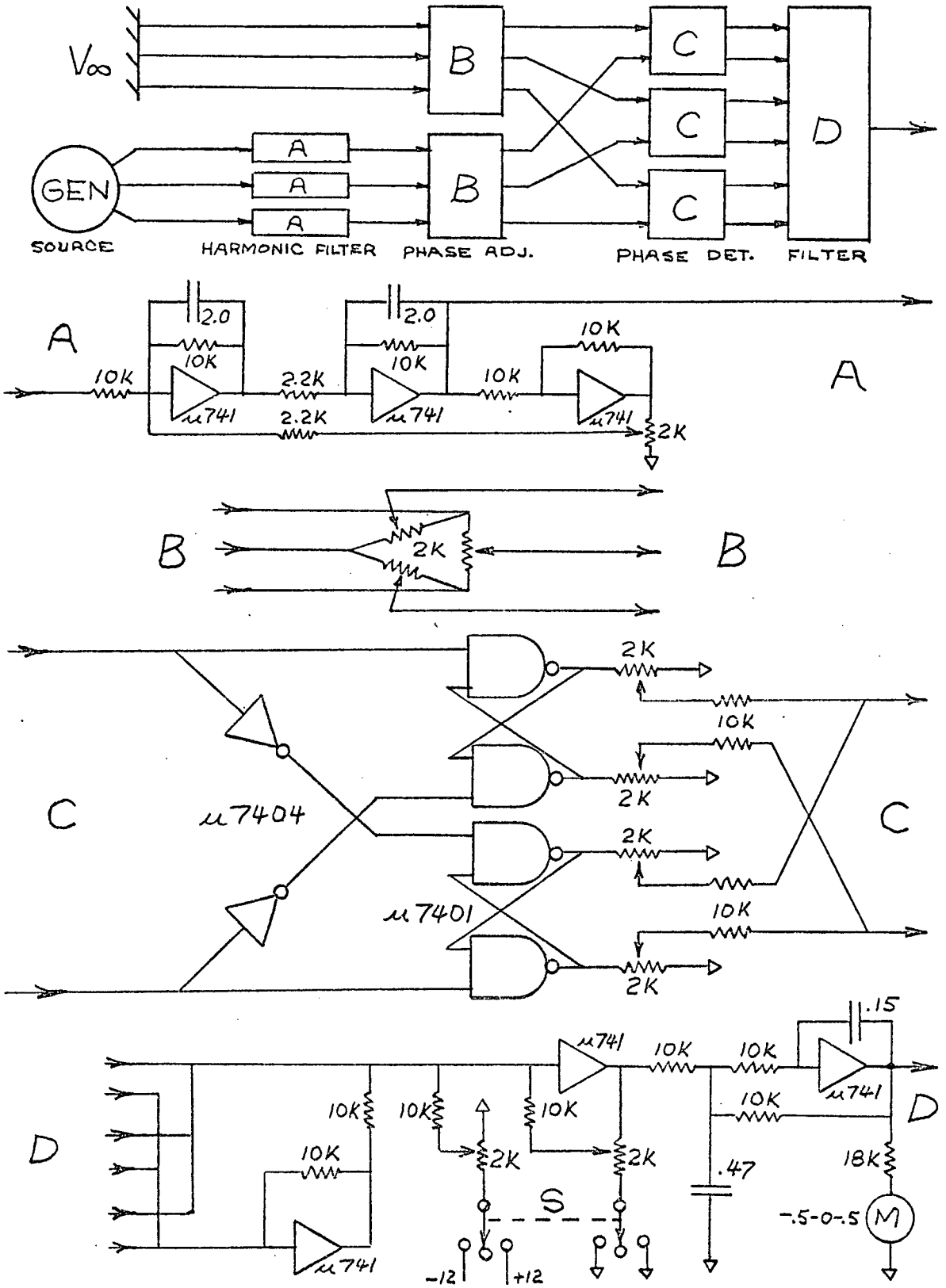

Figure 3.3 Wiring Schematic of Torque Angle Transducer

use heavy filtering to reduce the noise. The transducer designed for this model is a frequency demodulator driven from the same three phase 60 Hz alternator used for torque angle measurement.

The transducer has the following features:

1. linear characteristic in the range 377 $\pm$ 3.7 radian per second.
2. noise of 360 Hz under .1 radian per second.
3. time lage less than 20 msec.

An accurate true measure of deviation from synchronous speed is obtained by timing the cycling of the phase transducer through 360 degrees. This check on the linearity of the speed transducer is given by Figure 3.4.

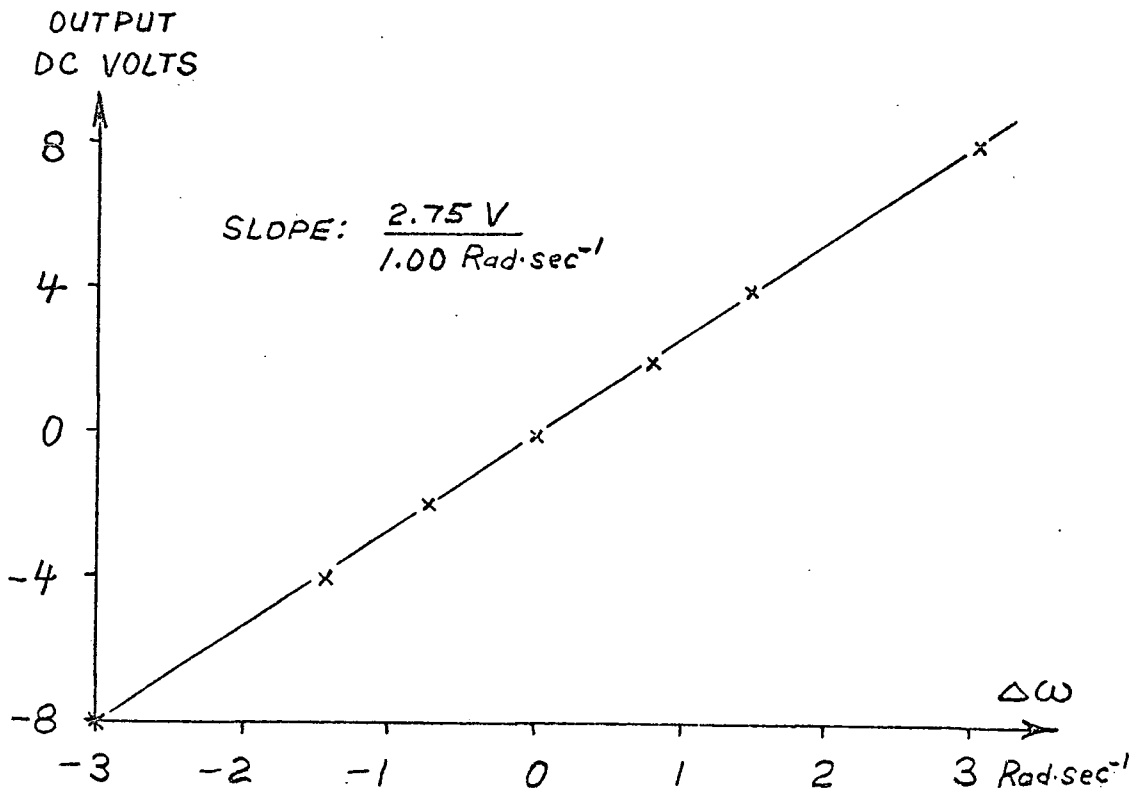

Figure 3.4 Speed Transducer Transfer Characteristic

The alternator frequency is demodulated using a Wien Bridge circuit with notch tuned to 60 Hz. The block diagram for one of three phases is given by Figure 3.5.

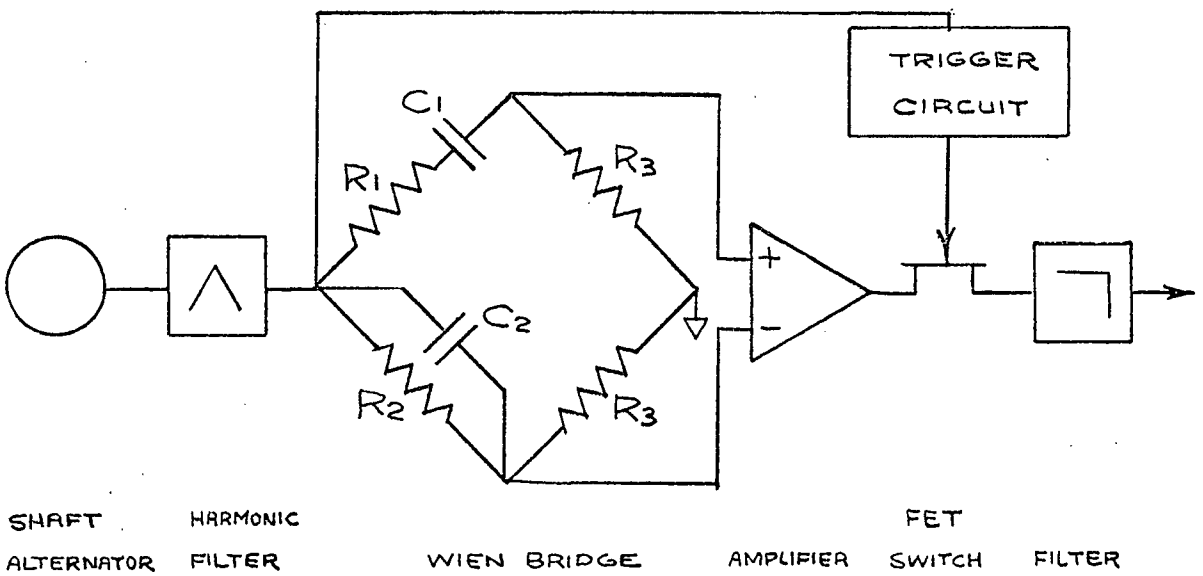

Figure 3.5 Block Diagram of Speed Transducer

At the center frequency, the series impedance R_1 and C_1 equals the parallel impedance R_2 and C_2, and the bridge output is theoretically zero. At other frequencies, the impedance is no longer equal and an ac output proportional to deviation results. The output phase, relative to the bridge input, leads by 90 degrees above center frequency and lags by 90 degrees below. The Field Effect Transistor analog transmission switch is controlled by the input signal resulting in phase sensitive rectification. Above 60 Hz, the transmission switch output is positive dc and below 60 Hz negative dc.

Harmonics of the input signal pass through the Wien Bridge and may overload the following amplifier. This is prevented with a preliminary filter adjusted to resonate at 60 Hz. The Q is limited to maintain the time lag under 20 msec.

Each of three phases uses the above circuitry to achieve a ripple in the output of 360 Hz which is removed in the final low pass filter. The transducer output is the product of alternator amplitude and frequency, both proportional to shaft speed. The error caused by this non-linearity is minor since the absolute speed change is small. The complete wiring schematic is given in Figure 3.6.

3.3 Terminal Voltage, Current and Power Transducers

For the voltage sensing, three potential transformers are connected line to line with secondaries rectified full wave resulting in 360 Hz ripple. The reference voltage is subtracted and the analog difference signal is filtered by a 12 dB per octave low pass filter with 60 Hz cutoff. Test results of linearity and sensitivity are shown in Figure 3.7.

For the current sensing, three transformers of 1:20 ratio are inserted in the line. The secondaries are connected to resistors which drop 20 volts with 10 amps on the primary. Rectification and filtering are similar to the voltage transducer with test results shown in Figure 3.8.

Instantaneous electrical power with no zero sequence is

$$P_e = v_{ac}\, i_a + v_{bc}\, i_b \qquad (3.1)$$

Two integrated circuit multipliers generate the power signal from voltage and current transformer inputs. The linearity as checked with

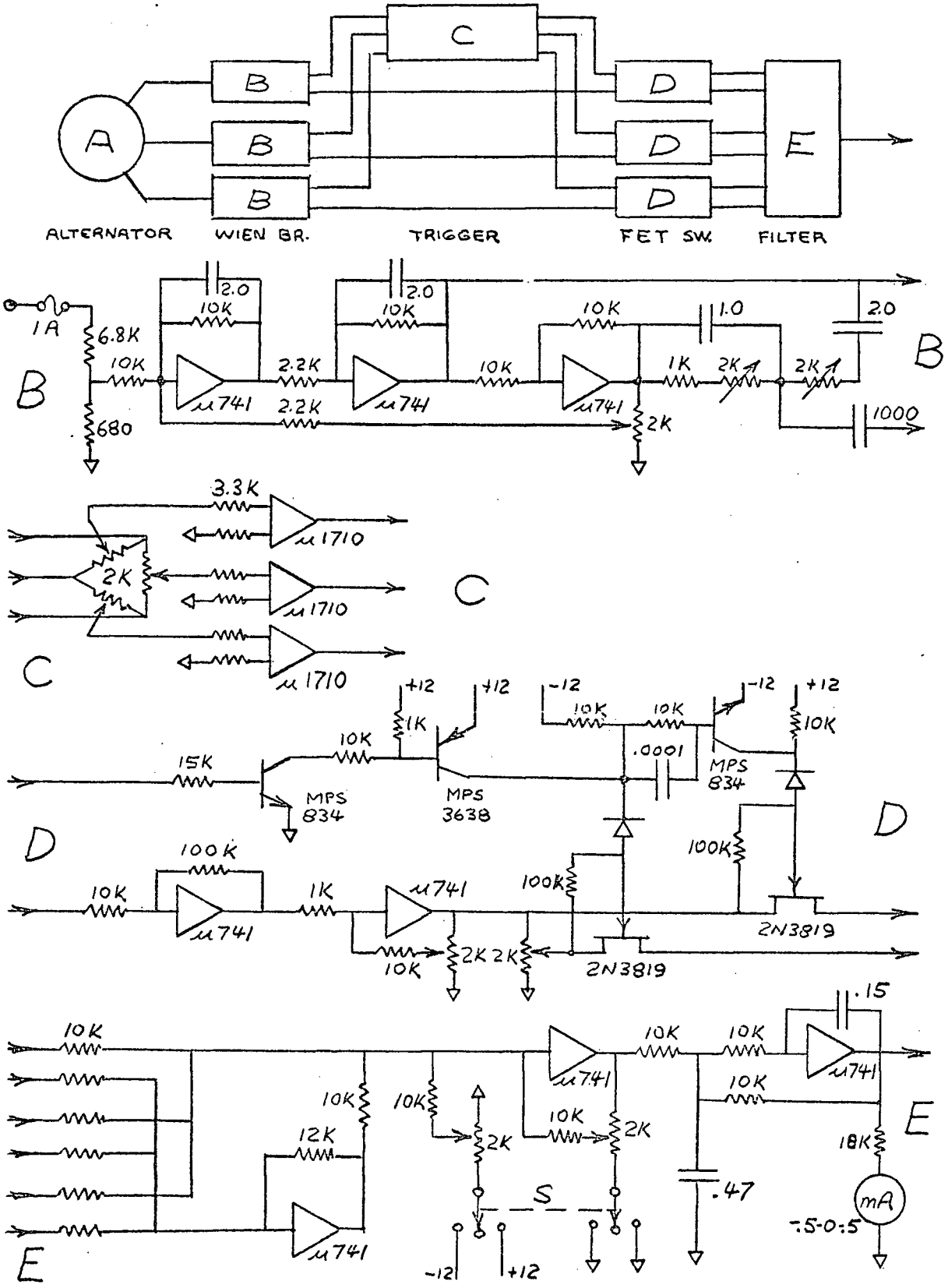

Figure 3.6 Wiring Schematic of Speed Transducer

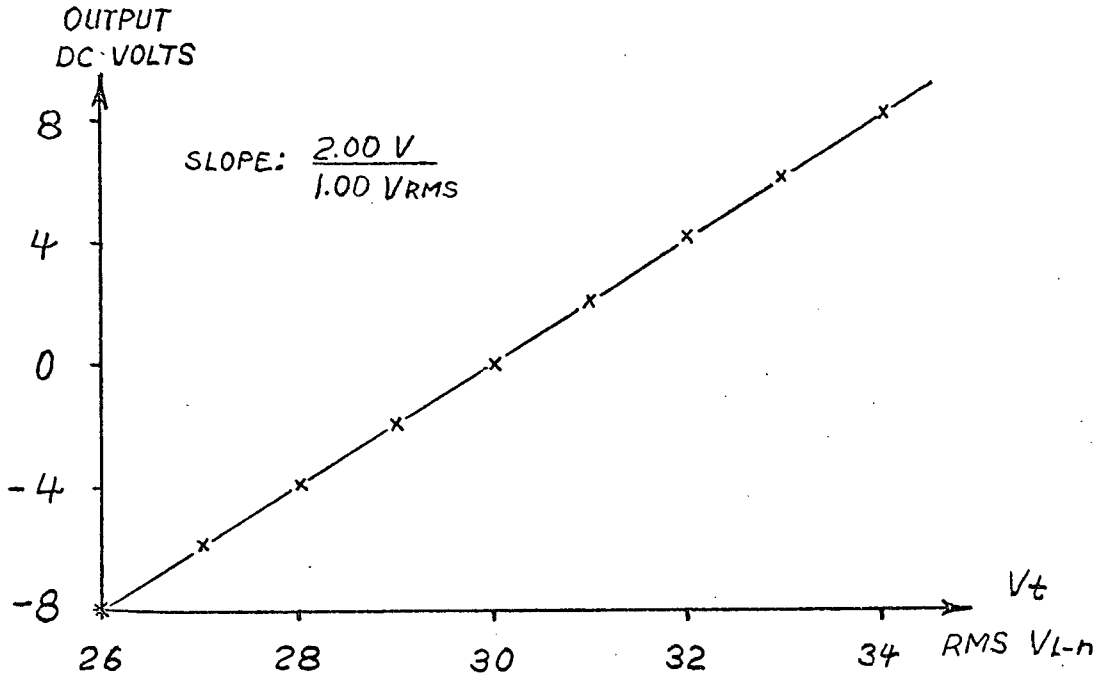

Figure 3.7 Voltage Transducer Transfer Characteristic

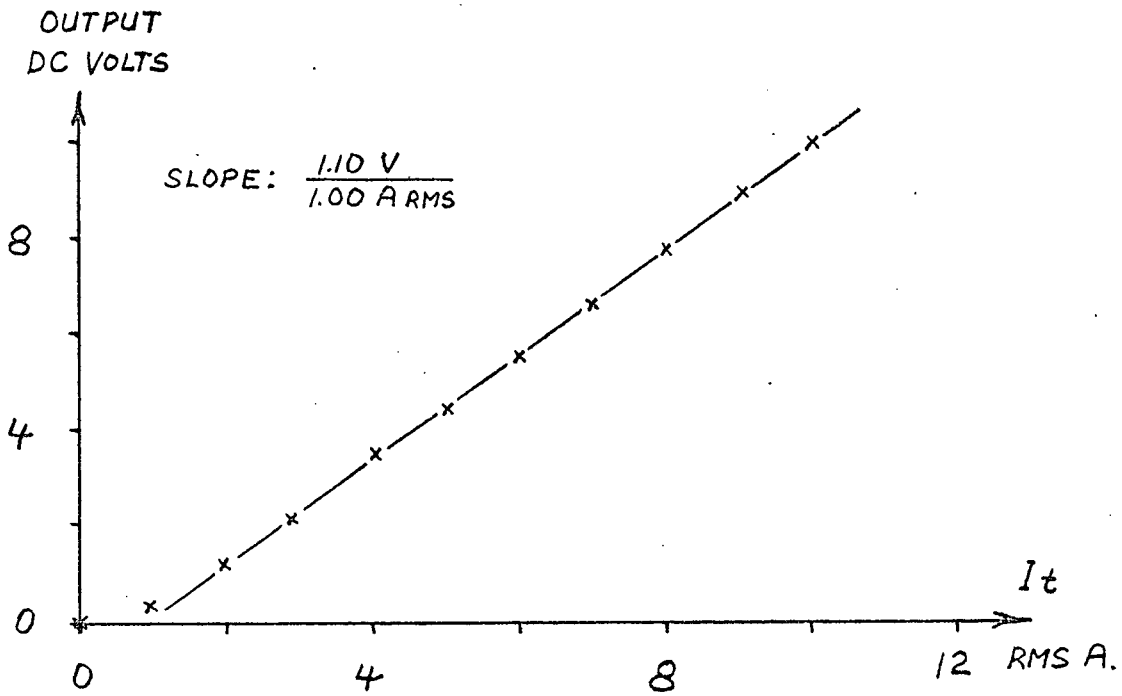

Figure 3.8 Current Transducer Transfer Characteristic

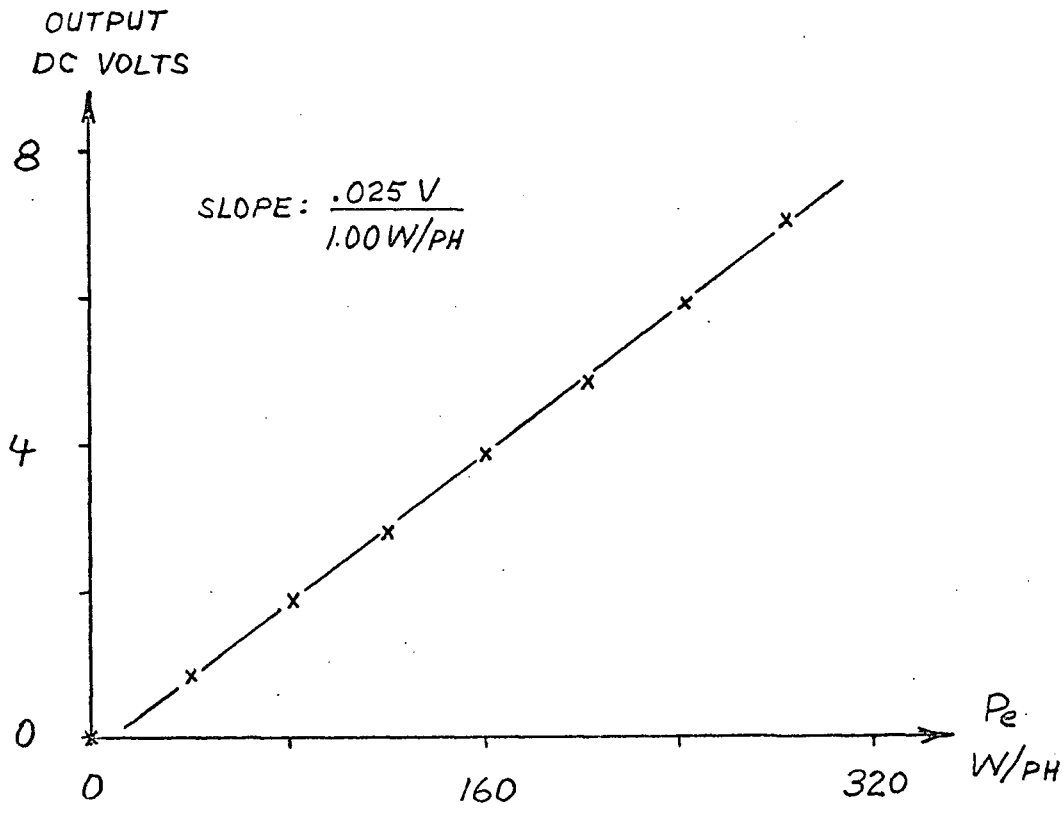

Figure 3.9 Power Transducer Transfer Characteristic

a wattmeter is confirmed by Figure 3.9.

3.4 Control Signal Compensation

Adjacent to the transducers is an analog panel with ten operational amplifiers and a patching board to simulate various phase and gain compensation schemes. Ten feedback signals, controlled by calibrated potentiometers, can be combined with positive or negative polarity to summing busses, feeding the direct and quadrature fields. Ten-turn reference potentiometers allow setting of the dc operating point. Provision is made for the exciter ceiling and time lag. The final control signals

for the two fields are displayed on meters.

3.5 Exciter and Field Time Constant Modification

For the exciter a Phase Linear "400" watt RMS stereo music amplifier is used. It is modified for dc operation as a dual channel, bipolar, programmable supply. The output rating is 60 volts at 4 amps but can be increased to 10 amps with forced air cooling.

The circuit of Figure 3.10 is used to artificially increase the field time constant of the generator by a factor of ten. A search coil with mutual inductance M is coupled to the field winding with resistance R_f and inductance L_f. Field current, i_f, passes through the sampling resistor R_x. The voltages on L_s and R_x are attenuated by potentiometers P_1 and P_2 and combined with input voltage, v_i, at the

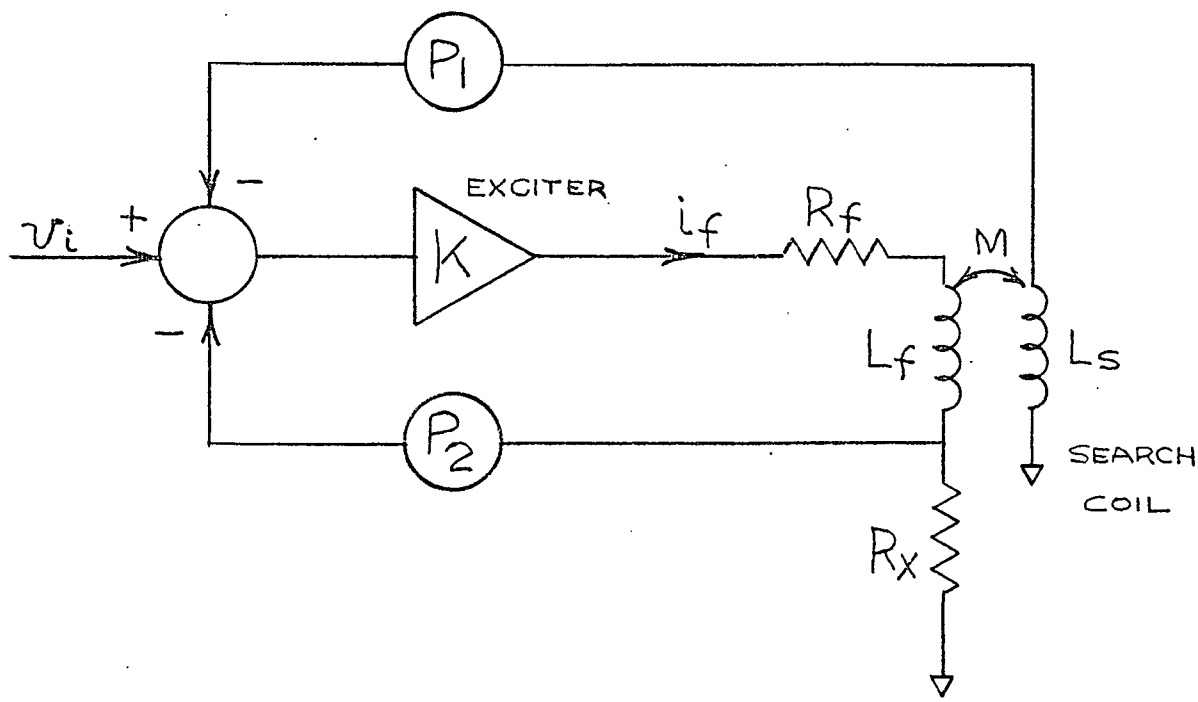

Figure 3.10 Time Constant Modification Circuit

high impedance input of the exciter with gain K. The relationship between v_i and i_f is

$$v_i = (P_2 R_x + \frac{R_f + R_x}{K}) i_f + (P_1 M + \frac{L_f}{K}) \frac{di_f}{dt} \qquad (3.2)$$

The first term represents the new equivalent resistance and the second term inductance. The exciter gain K is very large so the modified time constant is

$$T_f' = \frac{L_{f'}}{R_{f'}} \doteq \frac{P_1 M}{P_2 R_x} \qquad (3.3)$$

Armature circuits see the modified time constant through mutual coupling with the search coil. The method is inherently stable as actual field resistance R_f, which changes with heating, has little effect on Equation 3.3.

3.6 One-line Diagram of the Model Power System

Figure 3.11 gives a one-line diagram of the complete power system. The dc machine field rheostat R_1 controls shaft speed for synchronization and torque once the generator is synchronized. The armature voltage is adjusted by R_2 which influences the change in torque for a change in speed. Pulses of torque may be generated by a time delay relay S_1 and varied by R_3. These dynamic system disturbances are reproducible.

The operating point of the dual field generator is set by the voltmeter, ammeter and wattmeter and the control signals are available from the transducers. Switch S_2, with time delay reclosing, is provided for transient stability studies. The transmission line consists of 20 mH of lumped inductance with an extra 5 mH available when S_3 is open. A bank of three 1 KVA single phase transformers, connected Δ - Y,

steps up the voltage with 1:4 ratio. The delta primary allows a two-pole relay for S_2. The laboratory voltage supply is three phase 120/208 volts from B.C. Hydro.

For the stability experiments, a Sanborn two pen hot-wire recorder of 30 Hz frequency response is used to measure the phase relationship between feedback signals. This is backed up by a dual-beam storage oscilloscope. For the short circuit tests, the Honeywell Ultra-violet recorder capable of 3 KHz response is used.

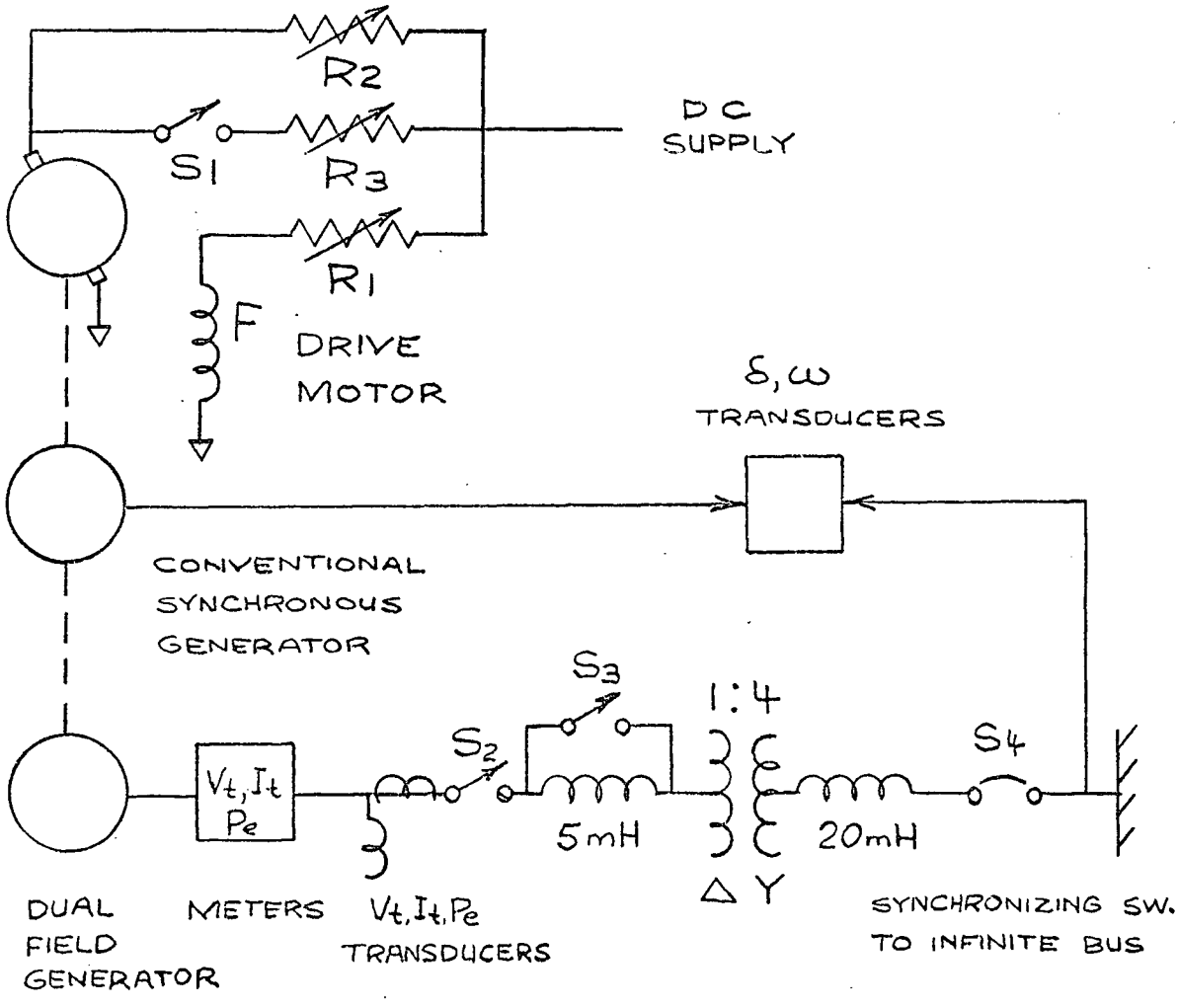

Figure 3.11 Power System One Line Diagram

4. EXCITATION CONTROL SCHEMES FOR ENHANCING SYSTEM DAMPING

This chapter develops an intuitive understanding of the supplemental excitation control design for increasing the mechanical damping of the machine. Torque angle, speed, power and terminal current signals are fed back to both direct and quadrature fields. Laboratory test and eigenvalue analysis results are given. The system eigenvalues are computed from equations derived in Chapter 5.

4.1 The System Under Study

A single machine is connected to an infinite bus through a medium length transmission line of constant impedance. The prime mover normally supplies constant torque with no governor effects included. Disturbances may be created in shaft torque for dynamic response studies.

There is only one voltage regulator which is used in the D field. The Q field is adjusted to be zero under steady state conditions. A stabilizer loop, similar to that used in reference [11], is modelled with an operational amplifier. The exciter ceiling voltage is $\pm$ 6 per unit in each axis. The voltage transducer and amplifier add a small time lag resulting in a voltage regulator of the second order. The loop gain through the regulator and machine is 390 K_{P1} where K_{P1} is a potentiometer setting which can be varied between 0. and 0.7. Figure 4.1 details the regulator block diagram.

The system operating point is chosen as follows. The infinite bus voltage is fixed at one per unit. The real power output of the system is set at 960 Watt where the machine hunting is a problem. The

corresponding torque angle, for the given transmission line, is close to 45 degrees. At this angle, D and Q fields are about equally effective

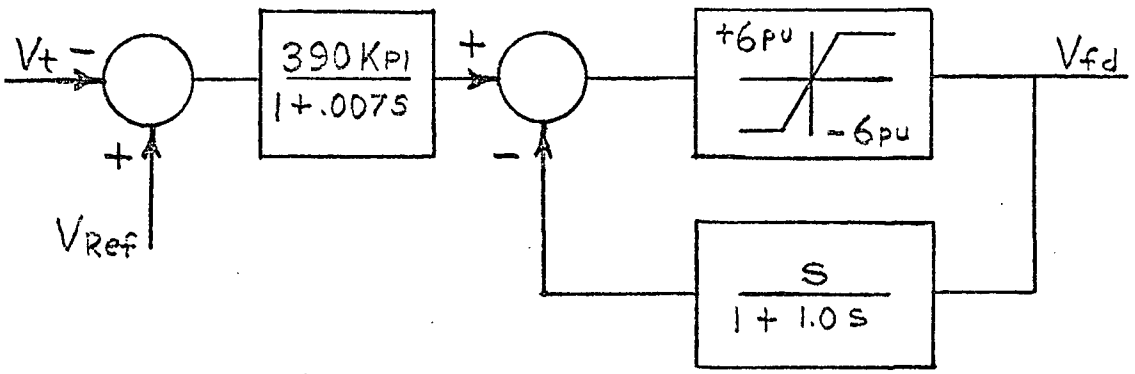

Figure 4.1 Block Diagram of the Voltage Regulator

in controlling the system dynamics [7]. A slightly leading reactive power is scheduled by adjusting the reference voltage of Figure 4.1. The precise operating values are listed in Table 4.1.

The voltage regulator improves the electric transient but not the dynamic stability of the system. Table 4.2 gives test and eigenvalue results for various regulator gains, K_{PI}. The damping coefficient, α, is the inverse of the time constant of shaft oscillations and is negative for stable systems. The damped frequency, ω_d, is in radians per second. An increase in ω_d indicates larger synchronizing torque. The difference between test and eigenvalue results is mainly due

Table 4.1

Operating Conditions, Per Unit

P	.90	v_t	1.01
Q	-.077	i_t	.91
v_o	1.00	i_{fd}	1.96
δ_o	43°	i_{fq}	0.0

Table 4.2

Voltage Regulator Effect on Mechanical Mode

Gain	Test Results		Eigenvalue Results	
K_{P1}	α	ω_d	α	ω_d
0.	-.65	11.9	-.48	10.6
.2	.24	11.9	.25	10.9
.3	.52	12.5	.39	11.1
.5	.82	12.9	.42	11.6

to errors in model and measurements. In particular, the feedback gain K_{P1} is calculated through many parameters. For the following supplementary control schemes, K_{P1} is held constant at .3. The loop gain of 120 is typical for modern voltage regulators and the system is unstable without further damping feedback.

4.2 Phase Plane Analysis

In deMello and Concordia's analysis [12] the block diagram transfer functions are evaluated at the mechanical resonant frequency. The

torque is resolved into damping and synchronizing components.

In this study δ, ω, P_e and i_t are available as transducer voltages which appear on the lower right part of Figure 4.2. Their effects on system damping are compared. The signals are obtained from

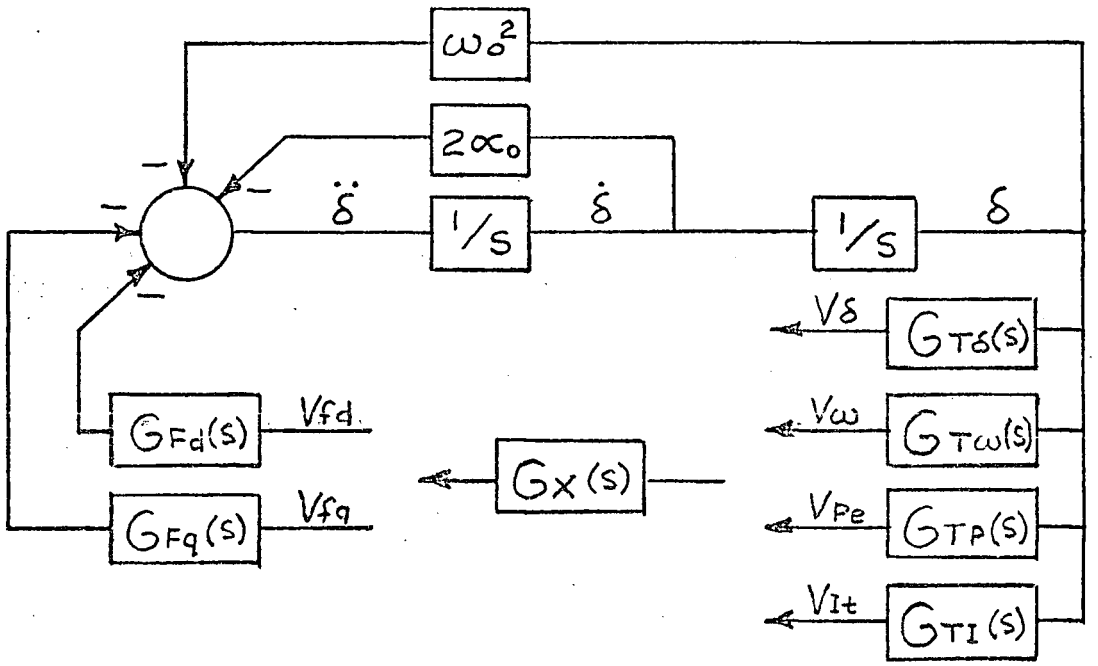

Figure 4.2 Block Diagram of the Phase Plane Model

transfer functions, $G_T(s)$, multiplying the instantaneous torque angle δ. An assumption is made that the closed loop effect on field voltage is small and may be neglected.

The feedback signals are compensated by individual blocks $G_X(s)$ and are applied to both D and Q field windings. The purpose is

to bring the supplemental electrical torque in phase with the speed providing a positive damping. Note that each field transfer function, $G_F(s)$, produces a gain and phase shift on the input signal.

The system with the voltage regulator but not the supplemental control is modelled by the upper part of Figure 4.2 resulting from the second order system of standard form

$$(s^2 + 2\alpha_o s + \omega_o^2)\delta = 0 \qquad (4.1)$$

The α_o and ω_o are constants measured at the operating point of the system.

The transfer functions $G_T(s)$ and $G_F(s)$ are experimentally determined at the mechanical oscillation frequency as follows. The system is made marginally stable with a speed signal roughly compensated and fed to the Q field. A signal generator, adjusted to the mechanical resonance, is also connected to the Q field to maintain machine oscillations at a constant amplitude. The magnitude relation between V_δ and V_ω, V_{Fe}, V_{it} is measured by a dual channel oscilloscope. Phase difference is determined by the Lissajous method. $G_{T\delta(s)}$ is known from the torque angle transducer sensitivity described in Chapter 3, assuming no phase shift due to the small time constants. Then $G_{T\omega(s)}$, $G_{TP(s)}$, and $G_{TI(s)}$ can be calculated with results listed in Table 4.3.

At mechanical resonance, the electrical torque produced by the oscillator is 180 degrees out of phase with speed. The angle between oscillator voltage and shaft speed can be directly measured on the oscilloscope. Thus the phase shift of the transfer functions $G_{Fd(s)}$ and $G_{Fq(s)}$ can be determined. Similarly the magnitude of $G_{Fd(s)}$ and $G_{Fq(s)}$ can be calculated from the voltage required to maintain the measured speed swing and the damping coefficient α_o.

Table 4.3

Gain and Phase Shift of Transfer Functions

G_{Fd}	$1.3\angle -40$ Rad/Volt Sec^2	$G_{T\omega}$	$29.8\angle 90$ Volt/Rad
G_{Fq}	$1.5\angle -90$ "	G_{TP}	$14.3\angle 0$ "
$G_{T\delta}$	$9.55\angle 0$ Volt/Rad	G_{TI}	$23.9\angle 0$ "

The D field has less phase lag than the Q field because of the negative feedback of the voltage regulator. The speed leads torque angle by 90 degrees as expected. Power and terminal current are in phase with torque angle since

$$\Delta P = \frac{VE}{x_s} \cos \delta \, \Delta\delta \tag{4.2}$$

when V and E are held constant and

$$\Delta I = \frac{\Delta P}{V \cos\theta} \tag{4.3}$$

when V cosθ is held constant. In the following sections, the compensation $G_{X(s)}$ is designed for each feedback scheme.

4.3 Torque Angle Feedback

A direct connection of V_{fq} to negative V_δ signal appears useful. Hopefully, the field lag brings electrical torque in phase with speed for positive damping. However, an experimental trial reveals that synchronization is lost for the following reason. A decrease in field current tends to increase the measured torque angle. When inverted and amplified by the proposed feedback scheme, the dynamic interaction aggravates the decrease in field current, leading to an instability of the system. The same situation holds for the direct axis field.

A solution is found by rolling off feedback gain, as on a

Bode plot, immediately below mechanical resonant frequency. Such a high pass filter contributes unavoidable phase lead at resonant frequency but can be tolerated for the Q field. Additional lag is necessary in the D axis. The filter schematic and phasor sketch are shown in Figure 4.3.

The compensation scheme has the following transfer function and phasor value at mechanical resonant frequency.

$$G_{Xd}(s) = \frac{-.14\ K_{P2}\ s^2}{(1+.2s)^2\ (1+.07s)},\quad G_{Xd}(s)\Big|_{s=j\omega_d} = 3.1\ K_{P2}\ \angle 164 \qquad (4.4)$$

$$G_{Xq}(s) = \frac{-.20\ K_{P2}\ s^2}{(1+.2s)^2},\quad G_{Xq}(s)\Big|_{s=j\omega_d} = 4.4\ K_{P2}\ \angle -136 \qquad (4.5)$$

Test and eigenvalue results are given in Table 4.4 for various feedback gains K_{P2}.

Table 4.4

Mechanical Mode of Torque Angle Feedback

	Gain	Test Results		Eigenvalue Results		
Axis	K_{P2}	α	ω_d	α	α'	ω_d
D	0.0	.52	12.5	.39	.39	11.1
"	.2	-.17	12.6	.06	.06	10.9
"	.4	-.95	12.0	-.32	-.32	10.7
"	.7	-4.0	7.0	-1.2	-1.2	10.2
Q	.1	.08	12.4	.05	.05	10.9
"	.2	-.28	12.5	-.36	-.36	10.6
"	.5	-2.2	12.6	-2.2	-1.5	10.2

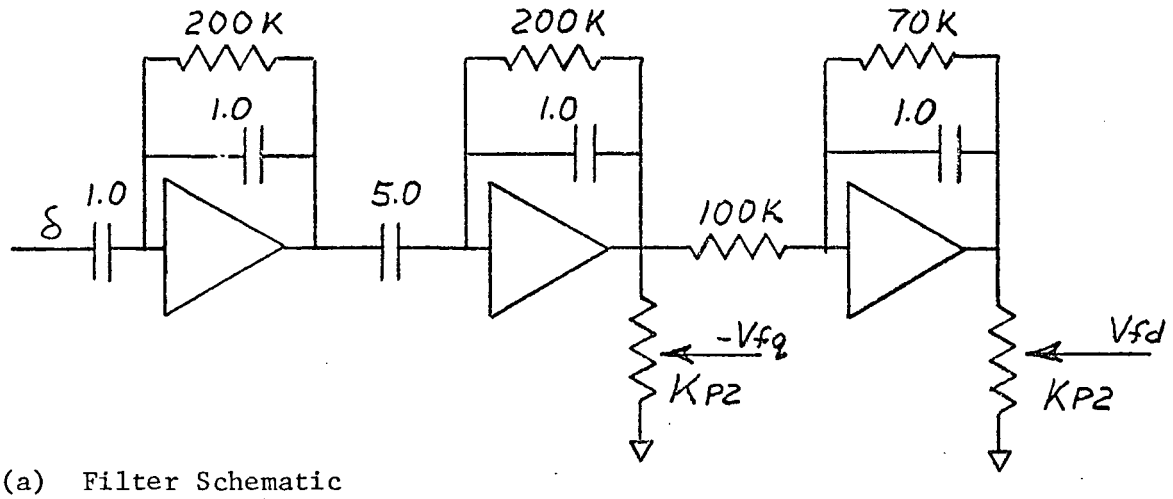

(a) Filter Schematic

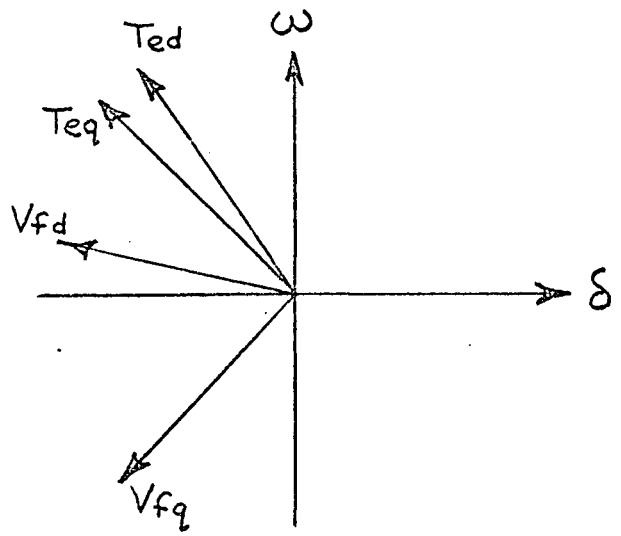

(b) Phasor Sketch

Figure 4.3 Torque Angle Signal Compensation

Good mechanical damping is achieved but low frequency electrical instability results for large gain. This is indicated by the real part of the most dominant eigenvalue, α', which becomes more positive than

the mechanical α.

4.4 Speed Feedback

Speed feedback requires lead compensation equal to the field lag. In the Q axis this amounts to 90 degrees and at least two amplifier stages are necessary. High frequency noise tends to be amplified more than the speed signal so a preliminary low pass filter is used. For the smaller lag of the D field, this filtering is made heavier to reduce the overall phase lead. The schematic and phasor sketch are shown in Figure 4.4.

The transfer function and phasor value at mechanical resonant frequency are

$$G_{Xd}(s) = \frac{.0056\ K_{P2}\ s^2}{(1+.07s)\ (1+.04s)^2}\ ,\ G_{Xd}(s)\Big|_{s=j\omega_d} = 1.23\ K_{P2} \angle 66 \qquad (4.6)$$

$$G_{Xq}(s) = \frac{.016\ K_{P2}\ s^2}{(1+.02s)\ (1+.04s)^2}\ ,\ G_{Xq}(s)\Big|_{s=j\omega_d} = 1.76\ K_{P2} \angle 112 \qquad (4.7)$$

Test and eigenvalue results are given in Table 4.5.

Table 4.5

Mechanical Mode of Speed Signal Feedback

	Gain	Test Results		Eigenvalue Results		
Axis	K_{P2}	α	ω_d	α	α'	ω_d
D	0.0	.52	12.5	.39	.39	11.1
"	.2	-.53	12.6	-.23	-.23	11.0
"	.4	-2.1	13.6	-1.4	-1.4	10.0
"	.7	-5.0	-	-2.3	-2.3	9.6

	Gain	Test Results		Eigenvalue Results		
Q	.2	-.73	12.5	.86	.86	10.4
"	.4	-2.5	12.5	-2.2	-2.2	8.9
"	.7	-4.0	-	12.	-8.6	-

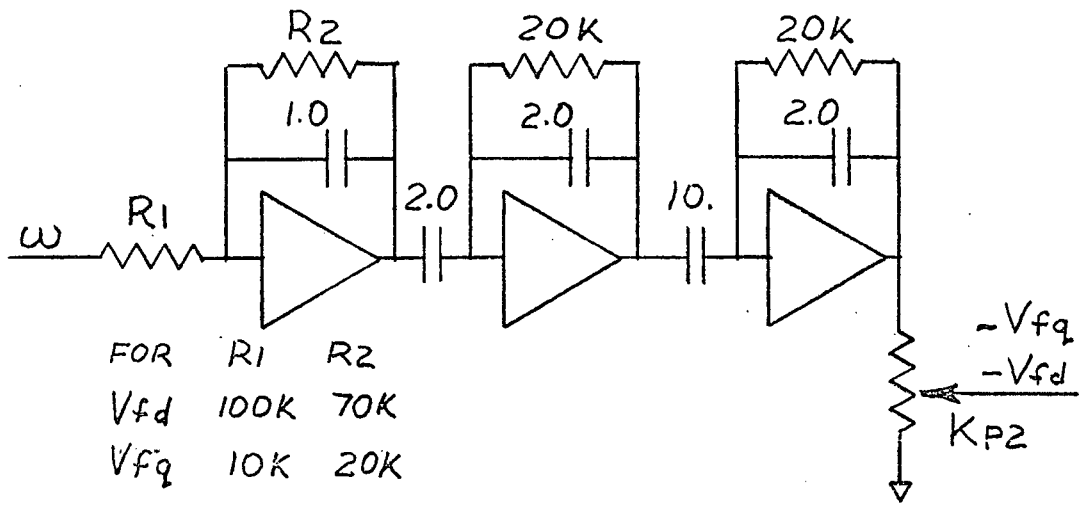

(a) Filter Schematic

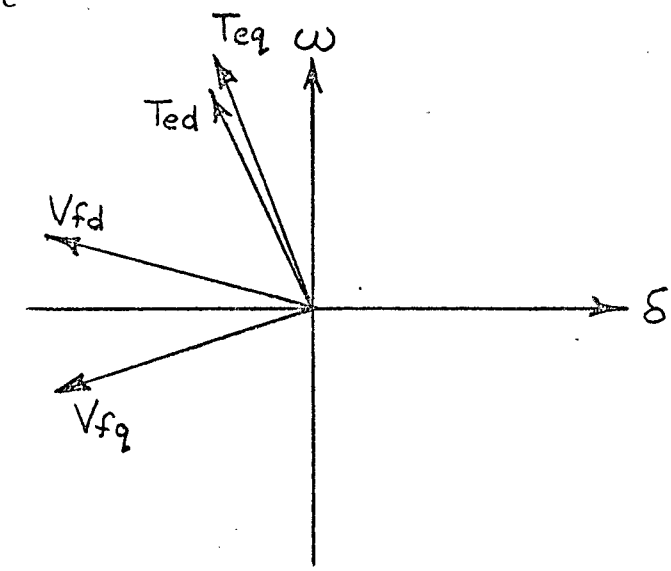

(b) Phasor Sketch

Figure 4.4 Speed Signal Compensation

Very good mechanical damping is achieved without the problem of low frequency instability.

4.5 Power Feedback

In Equation 4.2, electrical power is shown to be in phase with torque angle. The low frequency instability problem experienced with the torque angle scheme is reduced since steady state electrical power is independent of field current. Negative V_{Pe} signal is fed to the Q field and the 90 degree lag brings torque in phase with speed. A single low pass stage increases the D field lag to the same amount. A washout block removes any dc component from the power signal. The schematic and phasor sketch are shown in Figure 4.5.

The transfer function and phasor value at mechanical resonant frequency are

$$G_{Xd}(s) = \frac{-7\ K_{P2}\ s}{(1+1.0s)\ (1+.07s)},\quad G_{Xd}(s)\Big|_{s=j\omega_d} = 5.0\ K_{P2}\ \angle 120 \qquad (4.8)$$

$$G_{Xq}(s) = \frac{-10\ K_{P2}\ s}{(1+1.0s)},\quad G_{Xq}(s)\Big|_{s=j\omega_d} = 10.\ K_{P2}\ \angle 180 \qquad (4.9)$$

Test and eigenvalue results are given in Table 4.6.

Table 4.6

Mechanical Mode of Power Feedback

	Gain	Test Results		Eigenvalue Results		
Axis	K_{P2}	α	ω_d	α	α'	ω_d
D	0.0	.52	12.5	.39	.39	11.1
"	.1	-.51	12.6	-.76	-.76	10.9
"	.2	-1.9	13.6	-2.2	-1.04	10.2
"	.3	-5.0	-	-8.0	-1.02	12.5

	Gain	Test Results		Eigenvalue Results		
Q	.1	-1.07	12.5	-4.4	-.88	11.6
"	.2	-2.0	13.8	-9.8	-.87	12.8
"	.4	-11.	-	-20.	-.84	13.1

Mechanical damping is good but low frequency instability limits the useful gain.

4.6 Terminal Current Feedback

For small signal conditions, terminal current behaves like power and the compensation scheme of the previous section is duplicated. Current feedback may be useful during transients since fault current increases while power decreases from normal levels. The proper combination should enhance transient stability. Test and eigenvalue results for current feedback are given in Table 4.7.

Table 4.7

Mechanical Mode of Terminal Current Feedback

	Gain	Test Results		Eigenvalue Results		
Axis	K_{P2}	α	ω_d	α	α'	ω_d
D	0.0	.52	12.5	.39	.39	11.1
"	.1	-1.1	12.6	-1.2	-.73	10.9
"	.15	-2.1	13.0	-2.4	-.70	10.9
"	.2	-2.3	13.6	-3.8	-.67	11.2
Q	.1	-1.3	12.5	-1.7	-1.1	11.2
"	.2	-1.9	12.5	-4.0	-1.1	10.8
"	.4	-11.	-	-9.4	-1.0	8.3

As with power feedback, good damping is achieved but gain is limited

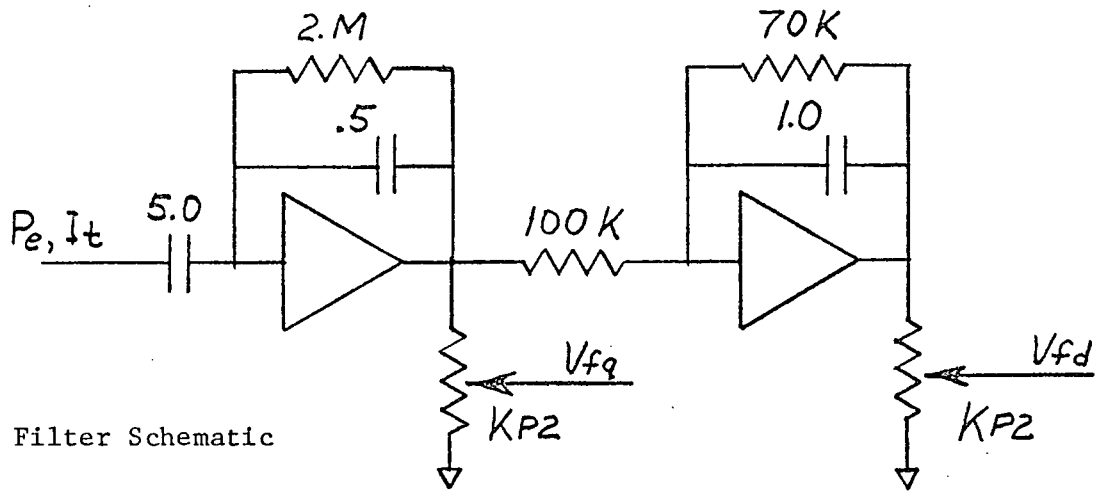

a) Filter Schematic

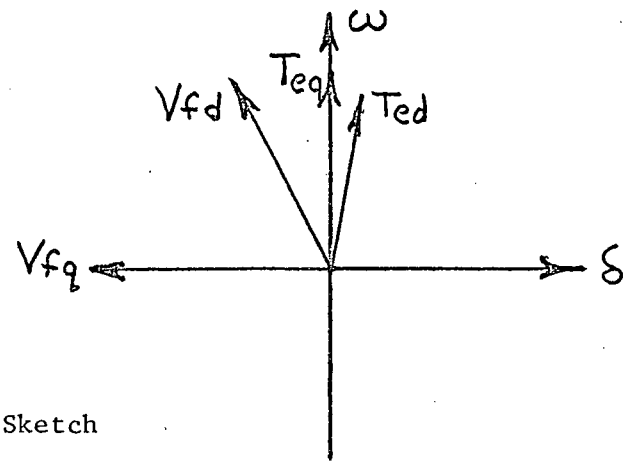

b) Power Phasor Sketch

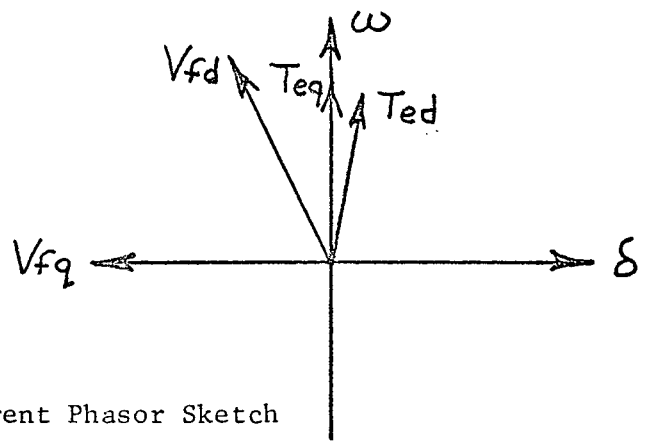

c) Terminal Current Phasor Sketch

Figure 4.5 Power and Terminal Current Compensation

by low frequency instability.

4.7 Comparison of Schemes

With any of the previous feedback signals, critical damping can be achieved for the mechanical oscillations, if electrical oscillations at other frequencies are not considered. An optimum feedback gain is realized when electrical poles instead of mechanical poles become the most dominant. Figure 4.6 plots negative α' against K_{P2} for the various schemes.

The transient performance cannot be judged by eigenvalue analysis alone. Test results reveal that complex filtering schemes delay the initiation of damping of the system. Table 4.8 lists the number of shaft swings before damping takes effect.

Table 4.8

Number of Transient Swings Before Damping

Axis	Feedback Source			
	δ	ω	P_e	i_t
D	1	1	1/2	1/2
Q	1	1/2	1/2	1/2

The dual field generator has a better performance in the low power, high leading power factor region as mentioned in the introduction. The sensitivity of each field in controlling dynamic torque is tested for various torque angles with results in Table 4.9. The D axis supplemental torque control is more effective at large torque angles whereas the Q axis control is better near zero output power. However, stability is not usually a great problem at light loads.

Another benefit of dual axis control is better terminal

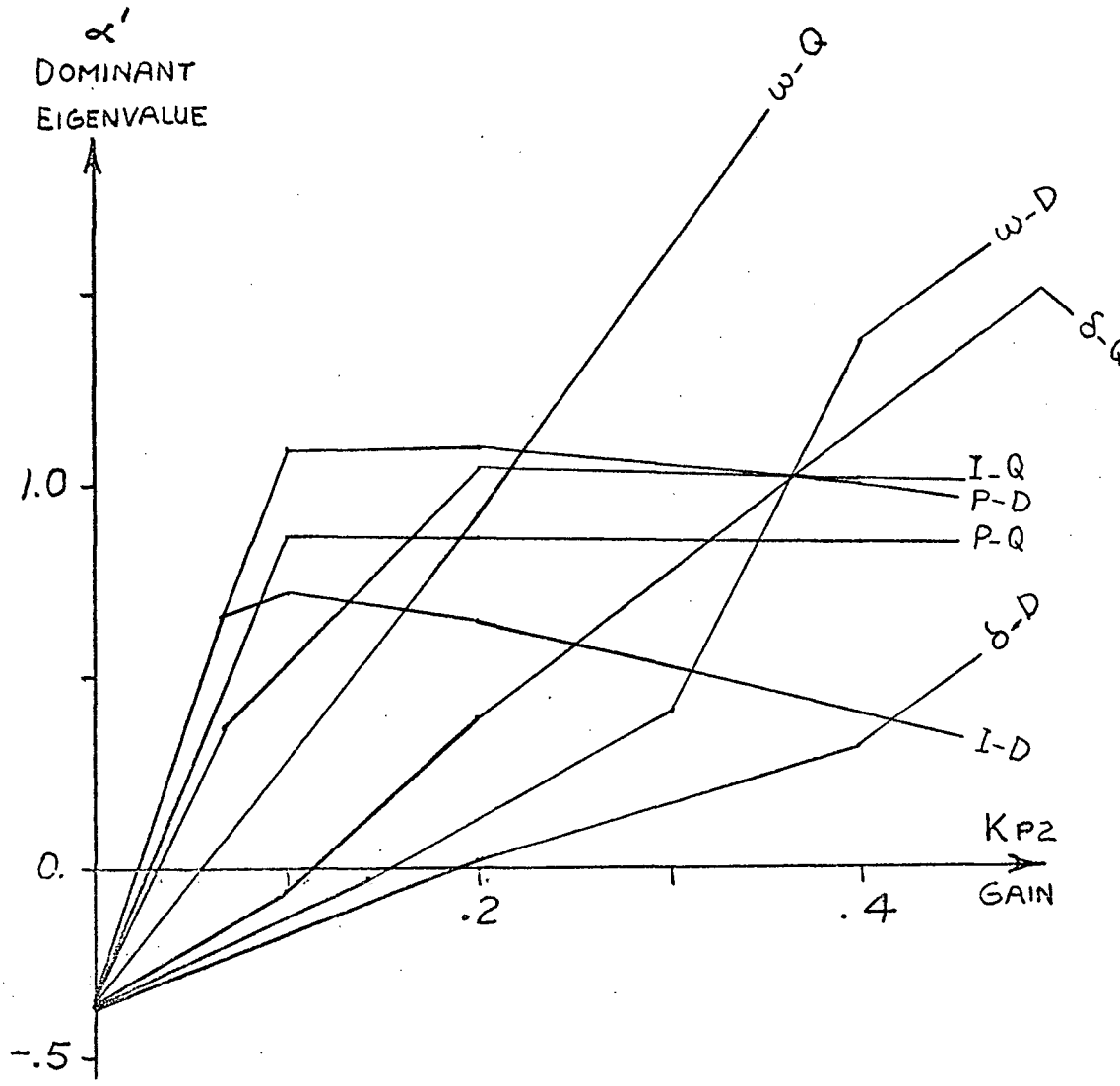

Figure 4.6 Comparison of Feedback Source and Axis

voltage regulation during swings. The induced voltage, which is related to direct field current, may be strongly affected by D axis damping schemes. Meanwhile, the Q field flux can change by significant amounts near the zero operating point without affecting the total field flux magnitude. Table 4.10 describes the change in terminal voltage per radian shaft swing for various feedback schemes. The results show the

superiority of the Q field in improving voltage regulation.

Table 4.9

D and Q Field Dynamic Torque Control

Torque Angle (degrees)	Normalized Sensitivity $(\frac{T_e}{V_f})$	
	D axis	Q axis
-26.	0.	.82
-13.	.22	.85
0.	.61	1.00
13.	.68	.67
26.	.93	.70
42.	1.27	.74

Table 4.10

Terminal Voltage Swing per Radian Shaft Swing

	Scheme				
Axis	None	δ	ω	P_e	i_t
D	6.8	11.4	12.3	12.7	9.1
Q	6.8	5.8	8.6	6.1	5.7

5. BASIC EQUATIONS OF THE DUAL-EXCITED MACHINE

A fourth order flux linkage model derived from basic synchronous machine equations is used for the study. Including the feedback control schemes, the resulting system equations are linearized and the system matrix is found. Eigenvalue results are compared with the tested results of Chapter Four.

5.1 Voltage and Flux Linkage Equations

The following assumptions are made in this analysis:

1. Q axis leading.
2. Constant voltage due to speed.
3. No saturation.
4. Armature transients neglected.
5. Damper circuits neglected.

Applying Park's transformation, the D axis equations in MKS units are:

$$\begin{bmatrix} V_{fd} \\ V_d - U_d \end{bmatrix} = \left(\begin{bmatrix} R_{fd} & 0 \\ 0 & R_a \end{bmatrix} + \frac{p}{\omega_o} \begin{bmatrix} X_{ffd} & \frac{3}{2} X_{fad} \\ X_{afd} & X_d \end{bmatrix} \right) \begin{bmatrix} I_{fd} \\ -I_d \end{bmatrix} \tag{5.1}$$

where $$U_d = \omega \Psi_q \tag{5.1a}$$

and U_d is the speed voltage and Ψ_q the flux linkage, both in MKS units.

When an invariant base power is chosen for both armature and field circuits, the X matrix will be symmetric. Thus the flux linkage becomes in per unit

$$\begin{bmatrix} \psi_{fd} \\ \psi_d \end{bmatrix} = \begin{bmatrix} x_{fd} & x_{md} \\ x_{md} & x_d \end{bmatrix} \begin{bmatrix} i_{fd} \\ -i_d \end{bmatrix} \tag{5.2}$$

Equation (5.1) is now

$$\begin{bmatrix} v_{fd} \\ v_d - u_d \end{bmatrix} = \begin{bmatrix} r_{fd} & 0 \\ 0 & r_a \end{bmatrix} \begin{bmatrix} i_{fd} \\ -i_d \end{bmatrix} + \frac{p}{\omega_o} \begin{bmatrix} \psi_{fd} \\ \psi_d \end{bmatrix} \tag{5.3}$$

The Q axis circuit equations are of similar form. For a leading Q axis the generated voltages are

$$\begin{aligned} u_d &= -\frac{\omega}{\omega_o} \psi_q \\ u_q &= +\frac{\omega}{\omega_o} \psi_d \end{aligned} \tag{5.4}$$

In view of the assumptions made, ω equals ω_o and $p\psi_d$, $p\psi_q$ can be neglected. Equation (5.3) and (5.4) can be written in state form

$$\frac{p}{\omega_o} \begin{bmatrix} \psi_{fd} \\ \psi_{fq} \end{bmatrix} = \begin{bmatrix} -r_{fd} & 0 \\ 0 & -r_{fq} \end{bmatrix} \begin{bmatrix} i_{fd} \\ i_{fq} \end{bmatrix} + \begin{bmatrix} v_{fd} \\ v_{fq} \end{bmatrix} \tag{5.5}$$

where

$$\begin{bmatrix} \psi_{fd} \\ \psi_d \\ \psi_{fq} \\ \psi_q \end{bmatrix} = \begin{bmatrix} x_{fd} & x_{md} & 0 & 0 \\ x_{md} & x_d & 0 & 0 \\ 0 & 0 & x_{fq} & x_{mq} \\ 0 & 0 & x_{mq} & x_q \end{bmatrix} \begin{bmatrix} i_{fd} \\ -i_d \\ i_{fq} \\ -i_q \end{bmatrix} \tag{5.6}$$

and

$$\begin{bmatrix} \psi_d \\ \psi_q \end{bmatrix} = \begin{bmatrix} 0 & r_a \\ -r_a & 0 \end{bmatrix} \begin{bmatrix} i_d \\ i_q \end{bmatrix} + \begin{bmatrix} v_q \\ -v_d \end{bmatrix} \tag{5.7}$$

The per unit parameter values are calculated from the base quantities listed in Table 5.1 and measurements obtained in Chapter 2.

Results are given in Table 5.2.

Table 5.1

Per Unit Base Quantities of the Machine

V_{nb}	45.3 V peak	defined by infinite bus voltage
I_{nb}	15.6 A peak	defined by machine rating
Z_{nb}	2.91 Ω	
I_{fb}	1.76 A	defined by short circuit ratio
V_{fb}	603 V	defined by power invariance
Z_{fb}	342 Ω	

Table 5.2

Per Unit Machine Parameters

r_a	.062		
x_d	.74	x_q	.68
x_d'	.41	x_q'	.41
T_{do}'	2.3 sec	T_{qo}'	2.3 sec

The mutual reactances are derived from the open circuit ratio:

$$x_{md} = \frac{X_{afd}\, I_{fd}}{V_{nb}} = .61$$

$$x_{mq} = \frac{X_{afq}\, I_{fb}}{V_{nb}} = .55 \qquad (5.8)$$

field inductance from the transient reactance:

$$x_{fd} = \frac{x_{md}^2}{x_d - x'_d} = 1.13$$

$$x_{fq} = \frac{x_{mq}^2}{x_q - x'_q} = 1.12 \qquad (5.9)$$

and field resistance from the open circuit field time constant:

$$r_{fd} = \frac{x_{fd}}{377\ T'_{do}} = .0013$$

$$r_{fq} = \frac{x_{fq}}{377\ T'_{qo}} = .0013 \qquad (5.10)$$

5.2 Torque Equations of the Machine

In MKS units, the electrical torque

$$T_e = \frac{3}{2}\ (I_q\ \Psi_d - I_d\ \Psi_q) \qquad (5.11)$$

The resulting shaft acceleration with torques at electrical angular velocity

$$p\omega = \frac{1}{J}\ (T_m - \frac{3}{2}\ I_q\ \psi_d + \frac{3}{2}\ I_d\ \psi_q - D\omega) \qquad (5.12)$$

The base torque chosen

$$T_b = \frac{3}{2}\ \frac{I_{nb}\ V_{nb}}{377} \qquad (5.13)$$

Equation (5.12) in per unit and linear form becomes

$$p\omega = K_j\ (t_m - i_{qo}\psi_d - i_q\psi_{do} + i_{do}\psi_q + i_d\psi_{qo} - d\omega) \qquad (5.14)$$

where

$$K_j = \frac{3\ I_{nb}\ V_{nb}}{2\ 377\ J} = 71.,\quad d = \frac{2\ 377\ D}{3\ I_{nv}\ V_{nb}} = .010 \qquad (5.14a)$$

All variables are understood to be incremental quantities. The second differential equation relates angular velocity in radians per second and torque angle in radians

$$p\ \delta = \omega \qquad (5.15)$$

5.3 Transmission Line Equations

The single line diagram of Chapter 3 is modelled by a pi equivalent with one leg absorbed in the infinite bus as in Figure 5.1. With transformer losses included in b and g, short circuit and open circuit tests define the parameter values which are given in per unit.

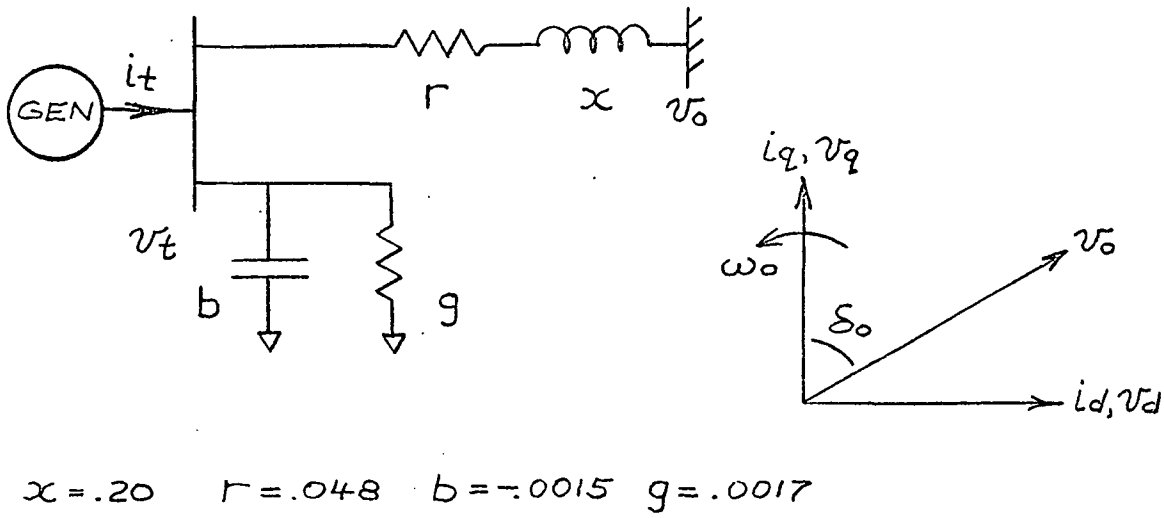

Figure 5.1 Transmission Line Sketch and Phasor Diagram

By inspection

$$i_t = (g + jb)\, v_t + \frac{v_t - v_o}{r + jx} \tag{5.16}$$

Dividing into components along the D and Q axis

$$\begin{bmatrix} (1+rg-xb) & -(rb+xg) \\ (rb+xg) & (1+rg-xb) \end{bmatrix} \begin{bmatrix} v_d \\ v_q \end{bmatrix} = \begin{bmatrix} v_o \sin\delta \\ v_o \cos\delta \end{bmatrix} + \begin{bmatrix} r & -x \\ x & r \end{bmatrix} \begin{bmatrix} i_d \\ i_q \end{bmatrix} \tag{5.17}$$

The matrix equation is inverted to solve for v_d, v_q

$$\begin{bmatrix} v_d \\ v_q \end{bmatrix} = \begin{bmatrix} K_1 & K_2 \\ -K_2 & K_1 \end{bmatrix} \begin{bmatrix} v_o \sin\delta \\ v_o \cos\delta \end{bmatrix} + \begin{bmatrix} (K_1 r + K_2 x)(-K_1 x + K_2 r) \\ -K_2 r + K_1 x)(K_2 x + K_1 r) \end{bmatrix} \begin{bmatrix} i_d \\ i_q \end{bmatrix} \tag{5.18}$$

where

$$K_1 = \frac{1-xb+rg}{\Delta}, \quad K_2 = \frac{xg+rb}{\Delta}, \quad \Delta = (1-xb+rg)^2 + (xg+rb)^2 \tag{5.18a}$$

5.4 Open Loop System Equations

The machine equations are of fourth order, two from Equation (5.5) and one each from Equations (5.14) and (5.15) with states: ψ_{fd}, ψ_{fq}, ω, δ. Auxiliary equations (5.6), (5.7) and (5.18) are combined to eliminate ψ_d, ψ_q, v_d, v_q.

$$\begin{bmatrix} \psi_{fd} \\ \psi'_d \\ \psi_{fq} \\ \psi'_q \end{bmatrix} = \begin{bmatrix} x_{fd} & x_{md} & 0 & 0 \\ x_{md} & x_{22} & 0 & x_{24} \\ 0 & 0 & x_{fq} & x_{mq} \\ 0 & x_{42} & x_{mq} & x_{44} \end{bmatrix} \begin{bmatrix} i_{fd} \\ -i_d \\ i_{fq} \\ -i_q \end{bmatrix} \tag{5.19}$$

where

$$\begin{bmatrix} \psi'_d \\ \psi'_q \end{bmatrix} = \begin{bmatrix} -K_2 & K_1 \\ -K_1 & -K_2 \end{bmatrix} \begin{bmatrix} v_o \sin\delta \\ v_o \cos\delta \end{bmatrix}$$

$$\begin{aligned} x_{22} &= x_d - K_2 r + K_1 x \\ x_{24} &= r_a + K_2 x + K_1 r \\ x_{42} &= -r_a - K_2 x - K_1 r \\ x_{44} &= x_q - K_2 r + K_1 x \end{aligned} \tag{5.20}$$

in compact notation

$$\underline{\psi}' = X\,\underline{i} \tag{5.19a}$$

Equation (5.20) is linearized

$$\begin{bmatrix} \psi'_d \\ \psi'_q \end{bmatrix} = \begin{bmatrix} g_1\,\delta \\ g_2\,\delta \end{bmatrix} \tag{5.21}$$

where

$$\begin{aligned} g_1 &= (-K_2 \cos\delta_o - K_1 \sin\delta_o)\, v_o \\ g_2 &= (-K_1 \cos\delta_o + K_2 \sin\delta_o)\, v_o \end{aligned} \tag{5.21a}$$

The subscript 'o' indicates the initial value of the variable.

The LHS of Equation (5.19) may also be defined by the state vector $\underline{x}$

$$\begin{bmatrix} \psi_{fd} \\ \psi'_d \\ \psi_{fq} \\ \psi'_q \end{bmatrix} = \begin{bmatrix} 1 & 0 & 0 & 0 \\ 0 & 0 & 0 & g_1 \\ 0 & 1 & 0 & 0 \\ 0 & 0 & 0 & g_2 \end{bmatrix} \begin{bmatrix} \psi_{fd} \\ \psi_{fq} \\ \omega \\ \delta \end{bmatrix} \tag{5.22}$$

or

$$\underline{\psi}' = Q\,\underline{x} \tag{5.22a}$$

Now $\underline{i}$ can be related to $\underline{x}$ through Equations (5.19) and (5.22)

$$\underline{i} = X^{-1}\,Q\,\underline{x} \tag{5.23}$$

The flux linkages ψ_d and ψ_q are found through Equation (5.6)

$$\begin{bmatrix} \psi_d \\ \psi_q \end{bmatrix} = \begin{bmatrix} x_{md} & x_d & 0 & 0 \\ 0 & 0 & x_{mq} & x_q \end{bmatrix} \underline{i} \tag{5.24}$$

or

$$\underline{\psi} = R\,\underline{i} \tag{5.24a}$$

The terminal voltage components from Equation (5.7)

$$\begin{bmatrix} v_d \\ v_q \end{bmatrix} = \begin{bmatrix} 0 & -1 \\ 1 & 0 \end{bmatrix} \underline{\psi} + \begin{bmatrix} 0 & r_a & 0 & 0 \\ 0 & 0 & 0 & r_a \end{bmatrix} \underline{i} \qquad (5.25)$$

or

$$\underline{v} = S\,\underline{\psi} + T\,\underline{i} \qquad (5.25a)$$

The linearized terminal parameters v_t, i_t, P_e are required for analyzing feedback schemes

$$\begin{bmatrix} v_t \\ i_t \\ P_e \end{bmatrix} = \begin{bmatrix} \frac{v_{do}}{v_{to}} & \frac{v_{qo}}{v_{to}} \\ 0 & 0 \\ i_{do} & i_{qo} \end{bmatrix} \underline{v} + \begin{bmatrix} 0 & 0 & 0 & 0 \\ 0 & \frac{-i_{do}}{i_{to}} & 0 & \frac{-i_{qo}}{i_{to}} \\ 0 & -v_{do} & 0 & -v_{qo} \end{bmatrix} \underline{i} \qquad (5.26)$$

or

$$\underline{t} = U\,\underline{v} + V\,\underline{i} \qquad (5.26a)$$

The state equations can be expressed from Equations (5.5), (5.14) and (5.15)

$$p\,\underline{x} = \begin{bmatrix} 0 & 0 & 0 & 0 \\ 0 & 0 & 0 & 0 \\ 0 & 0 & -d & 0 \\ 0 & 0 & 1 & 0 \end{bmatrix} \underline{x} + \begin{bmatrix} -\omega_o r_{fd} & 0 & 0 & 0 \\ 0 & 0 & -\omega_o r_{fq} & 0 \\ 0 & -K_j\psi_{qo} & 0 & K_j\psi_{do} \\ 0 & 0 & 0 & 0 \end{bmatrix} \underline{i} +$$

$$\begin{bmatrix} 0 & 0 \\ 0 & 0 \\ -K_j i_{qo} & -K_j i_{do} \\ 0 & 0 \end{bmatrix} \underline{\psi} \qquad (5.27)$$

or

$$p\,\underline{x} = C\,\underline{x} + D\,\underline{i} + E\,\underline{\psi} \tag{5.27a}$$

Equations (5.23) and (5.24) allow elimination of $\underline{i}$ and $\underline{\psi}$. The system 'A' matrix is found

$$p\,\underline{x} = A\,\underline{x} \tag{5.28}$$

where

$$A = C + D\,X^{-1}\,Q + ER\,X^{-1}\,Q \tag{5.28a}$$

The matrix multiplication is done with Fortran subroutines.

5.5 Calculation of Operating Point

The operating point is usually defined by P_o, Q_o, and v_{to} but in this study v_{to}, i_{to} and v_o are used because the infinite bus voltage is fixed. Equation (5.16) is rewritten as

$$i_{to} = v_{to}\,(g' + jb') - \frac{v_o}{r+jx} \tag{5.29}$$

where

$$g' + jb' = g + jb + \frac{1}{r+jx} \tag{5.29a}$$

Equation (5.29) may be represented by a triangle of phasors with γ the angle between i_{to} and $v_{to}\,(g' + b')$. Application of the cosine law gives

$$\gamma = \cos^{-1}\left[\frac{v_{to}^2\,(g'^2 + b'^2) + i_{to}^2 - \dfrac{v_o^2}{r^2+x^2}}{2\,i_{to}\,v_{to}\sqrt{g'^2 + b'^2}}\right] \tag{5.30}$$

From the definition of γ, the power factor and complex power are

$$\theta_o = -\tan\frac{b'}{g'} - \gamma\ , \qquad Q_o = v_{to}\,i_{to}\,\sin\theta_o$$
$$P_o = v_{to}\,i_{to}\,\cos\theta_o \tag{5.31}$$

Assuming v_{to} lags the machine Q axis with angle β, the terminal components are

$$\begin{aligned} v_{do} &= v_{to} \sin \beta \\ v_{qo} &= v_{to} \cos \beta \\ i_{do} &= i_{to} \sin (\beta+\theta_o) \\ i_{qo} &= i_{to} \cos (\beta+\theta_o) \end{aligned} \tag{5.32}$$

From Equations (5.6) and (5.7)

$$v_{do} = -x_{mq}\, i_{fqo} + x_q\, i_{qo} - r_a\, i_{do} \tag{5.33}$$

With Q field excitation zero in the steady state, i_{fqo} vanishes. Substituting Equation (5.32) in (5.33) and applying the trigonometric expansion formulas

$$\beta = \tan^{-1}\left[\frac{-r_a \sin\theta_o + x_q \cos\theta_o}{v_{to}/i_{to} + r_a \cos\theta_o + x_q \sin\theta_o}\right] \tag{5.34}$$

The terminal components of Equation (5.32) are evaluated, followed by δ_o and v_o from Equation (5.17). ψ_{do} and ψ_{qo} are obtained from Equation (5.7) followed by i_{fdo}, ψ_{fdo} and ψ_{fqo} from Equation (5.6).

5.6 Voltage Regulator Equations

The block diagram of the voltage regulator in Figure 4.1 is modelled by two transfer functions

$$\begin{aligned} x_1 &= \frac{390\, K_{P1}\, (-V_t + V_{REF})}{1 + .007\, s} \\ x_2 &= \frac{(1 + s)}{(1 + 2s)}\; x_1 \end{aligned} \tag{5.35}$$

where x_2 is summed with any D axis supplemental signal and applied to

the D field winding. Equation (5.35) is modified to incremental per unit quantities with open loop gain through the machine held constant

$$x_1 = \frac{-.88\ K_{P1}\ v_t}{1 + .007\ s}$$

$$x_2 = \frac{(1 + s)}{(1 + 2s)}\ x_1 \tag{5.36}$$

In state form

$$p\ x_1 = -\frac{x_1}{T_1} - \frac{.88\ K_{P1}\ v_t}{T_1}$$

$$p\ x_2 = -\frac{x_2}{T_3} + \frac{1}{T_3}\left(1 - \frac{T_2}{T_1}\right) x_1 - \frac{.88\ K_{P1}\ v_t}{T_1\ T_3} \tag{5.37}$$

where

$$T_1 = .007\ ,\quad T_2 = 1.0,\quad T_3 = 2.0 \tag{5.37a}$$

5.7 Supplemental Feedback Schemes for Damping

All of the feedback compensation schemes are modelled by the generalized transfer function

$$Gx(s) = \frac{K_T\ K_{P2}\ s^2}{(1 + T_4 s)(1 + T_5 s)(1 + T_6 s)} \tag{5.38}$$

The transducer gain K_T includes the scaling effect in converting to per unit while K_{P2} remains the potentiometer setting between 0. and .7. The parameter values for each scheme are given in Table 5.3.

The transfer function forms three state equations

$$p\ x_3 = \frac{-x_3}{T_4} + \frac{K_T\ K_{P2}\ u}{T_4}$$

$$p\ x_4 = \frac{-x_4}{T_5} - \frac{x_3}{T_4 T_5} + \frac{K_T\ K_{P2}\ u}{T_4\ T_5}$$

$$p\,x_5 = \frac{x_5}{T_6} - \frac{x_4}{T_5 T_6} - \frac{x_3}{T_4 T_5 T_6} + \frac{K_T\,K_{P2}\,u}{T_4\,T_5\,T_6} \tag{5.39}$$

Table 5.3

Compensation Scheme Parameter Values

Source	Axis	K_T	T_4	T_5	T_6
δ	D	-.0026	.07	.2	.2
δ	Q	-.0026	.007	.2	.2
ω	D	.000060	.07	.04	.04
ω	Q	.000060	.02	.04	.04
P_e	D	-.36	.07	1.0	1.0
P_e	Q	-.36	.007	1.0	1.0
I_t	D	-.165	.07	1.0	1.0
I_t	Q	-.165	.007	1.0	1.0

where u is the source δ, ω, P_e or I_t, and x_5 is the voltage applied to the D or Q field winding.

5.8 Closed Loop System Equations

The state vector is of ninth order (ψ_{fd}, ψ_{fq}, ω, δ, x_1, x_2, x_3, x_4, x_5) and Equation (5.27) is modified to include the closed loop

$$p\,\underline{x} = C\,\underline{x} + D\,\underline{i} + E\,\underline{\psi} + G\,\underline{t} \tag{5.40}$$

where for power feedback to the Q field, for example

$$C = \begin{bmatrix} 0 & 0 & 0 & 0 & 0 & \omega_o & 0 & 0 & 0 \\ 0 & 0 & 0 & 0 & 0 & 0 & 0 & 0 & \omega_o \\ 0 & 0 & -d & 0 & 0 & 0 & 0 & 0 & 0 \\ 0 & 0 & 1 & 0 & 0 & 0 & 0 & 0 & 0 \\ 0 & 0 & 0 & 0 & \frac{-1}{T_1} & 0 & 0 & 0 & 0 \\ 0 & 0 & 0 & 0 & \left(\frac{1}{T_3} - \frac{T_2}{T_1 T_3}\right) & \frac{-1}{T_3} & 0 & 0 & 0 \\ 0 & 0 & 0 & 0 & 0 & 0 & \frac{-1}{T_4} & 0 & 0 \\ 0 & 0 & 0 & 0 & 0 & 0 & \frac{-1}{T_4 T_5} & \frac{-1}{T_5} & 0 \\ 0 & 0 & 0 & 0 & 0 & 0 & \frac{-1}{T_4 T_5 T_6} & \frac{-1}{T_5 T_6} & \frac{-1}{T_6} \end{bmatrix} \tag{5.41}$$

$$G = \begin{bmatrix} 0 & 0 & 0 \\ 0 & 0 & 0 \\ 0 & 0 & 0 \\ 0 & 0 & 0 \\ \frac{-.88\ K_{P1}}{T_1} & 0 & 0 \\ \frac{-.88\ K_{P1} T_2}{T_1\ T_3} & 0 & 0 \\ 0 & 0 & \frac{K_T\ K_{P2}}{T_4} \\ 0 & 0 & \frac{K_T\ K_{P2}}{T_4\ T_5} \\ 0 & 0 & \frac{K_T\ K_{P2}}{T_4\ T_5\ T_6} \end{bmatrix} \tag{5.42}$$

Matrices D and E are unchanged from the open loop case. Equations (5.23), (5.24) and (5.25) are substituted in (5.40) to obtain the closed loop system matrix

$$A = C + \{D + ER + G[U(SR + T) + V]\} \quad X^{-1} \; Q \qquad (5.43)$$

The equation is evaluated and the eigenvalues found using available Fortran subroutines. The results are compared with the experimental tests as described in Chapter 4.

6. CONCLUSIONS

From laboratory test results and eigenvalue analysis of the dual field generator, the following conclusions are formed.

1. When operating close to rated output, the direct and quadrature fields are about equally effective in dynamically controlling the machine oscillations. At torque angles near zero, the quadrature field is superior.
2. Compensated speed signal provides the best damping for either field. No low frequency electrical instability appears for large feedback gains.
3. Power and terminal current signals provide good damping with very simple compensation. Large gains result in low frequency electrical instability.
4. Torque angle signal requires complex filtering for fair damping. The method is very sensitive to low frequency electrical instability.
5. Complex filtering or compensation schemes are undesirable. The initiation of damping is delayed. Lead compensation amplifies noise while lag compensation increases the tendancy to low frequency instability.
6. Terminal voltage regulation is less sensitive to shaft swings with dual field control.

Conclusions 1 and 6 agree with results in the literature [3, 5, 7].

The results of this thesis may be extended in the following areas:

1. Operation at constant torque angle for improved transient stability as in reference [5]. Provision is made on the model for transient line switching.
2. Study of a quadrature field with less turns. A major impediment to stability is the large field lag. Since the quadrature field does not need to supply continuous ampere-turns, its turns and inductance may be reduced. The field constant is easily changed on the model.
3. A more accurate block diagram with flux linkage parameters would improve the accuracy of design in Chapter 4. The flux linkage model in Chapter 5 is easily modified to sixth or eighth order machine equations for more accurate results. The problem is the measurement of the subtransient machine parameters as damper winding resistance is relatively high in the laboratory model.

The laboratory synchronous machine model could be improved with the following changes:

1. Reduce 11th and 13th harmonics by rounding the shoe tips to a radius of .32 cm.
2. Make the dc drive motor torque more constant with speed. The model damping is presently too large due to this factor.
3. Provide greater cooling on the exciter amplifier to extend the range of voltage ceiling.
4. Find and correct the cause of small drifts in torque angle. Change in brush resistance is suspected. The noise makes relatively large test swings necessary when checking small signal dynamic results. Errors are then caused by the field voltage reaching the upper limit.

REFERENCES

1. Hamdi-Sepen, C., "Process for increasing the transient stability power limits on ac transmission systems - Pt. 1", CIGRE, 1962, paper 305.

2. Botvinnik, M.M., "Asynchronized synchronous machine", (Pergamon, 1964).

3. Takata, S., "Compensation of bus voltage fluctuation by means of optimal control of synchronous machine excitation", J. Inst. Elec. Engrs. Japan, Vol. 88, No. 12, 1968, p. 42.

4. Takata, S., Ohta, E., and Naganuma, Y., "Suppression of hunting in two-axis synchronous machines by control of field voltage", J. Inst. Elec. Engrs. Japan, Vol. 88, No. 2, 1968, p. 28.

5. Soper, J.A., Fagg, A.R., "Divided-winding-rotor synchronous generator", Proc. IEE, Vol. 116, No. 1, p. 113.

6. Robinson, R.B., "Transient equivalent circuit of the divided-winding-rotor synchronous machine", Proc. IEE, Vol. 117, No. 3, p. 552.

7. Krause, P.C. and Towle, J.N., "Synchronous machine damping by excitation control with direct and quadrature axis field windings", IEEE PAS, Vol. 88, No. 8, 1969, p. 1266.

8. Subramaniam, P. and Malik, O.P., "Closed loop optimization of power systems with two-axis excitation control", IEEE Winter Meeting, 1972.

9. El-Serafi, A.M. and Badr, M.A., "Choice of the excitation system parameters for maximum possible capacitive power loading of dual-excited synchronous generators", IEEE Winter Meeting, 1973.

10. Kuhlmann, J.H., "Design of electrical apparatus", Wiley, 1950, p. 67 and Appdx. 1.

11. Yu, Y.N. and Habibullah, B., "Improving supplemental excitation control design using accurate model", IEEE Winter Meeting, 1973.

12. de Mello, F.P. and Concordia, C., "Concepts of synchronous machine stability as affected by excitation control", IEEE PAS, April, 1969, p. 316.